https://doi.org/10.5194/egusphere-2026-2961
Preprint. Discussion started: 2 June 2026

Aerosol–cloud interactions influence the climate response to AMOC weakening

Ryan Vella and Ulrike Lohmann

Institute for Atmospheric and Climate Science, ETH Zürich, Zurich, Switzerland

Correspondence: Ryan Vella (ryan.vella@env.ethz.ch)

Abstract.

The Atlantic Meridional Overturning Circulation (AMOC) strongly influences regional climate, yet the response of atmospheric aerosols and aerosol–cloud interactions to its weakening remains largely unexplored. Using the ICON-HAM model, we investigate how a 60 % AMOC weakening affects aerosol distributions, cloud microphysics, and radiative budgets. The weakening of the AMOC drives a hemispheric aerosol redistribution through purely dynamical pathways, increasing the Northern Hemisphere aerosol burden by 5 % through enhanced Saharan dust emissions and extended aerosol lifetimes under suppressed wet deposition. Averaged over 40–90°N, these perturbations propagate into cloud properties via both liquid and ice-phase pathways. In-cloud droplet number concentrations increase by 8 % in warm clouds and 13 % in the mixed-phase regime. In the ice phase, enhanced dust ice-nucleating particles produce a 37 % increase in mixed-phase ice crystal number concentrations through multiple heterogeneous freezing pathways, promoting the Wegener–Bergeron–Findeisen process and reducing mixed-phase total water path by 8 %. The global-mean net cloud radiative effect (CRE) anomaly is $+0.84\,\mathrm{W\,m^{-2}}$, acting as a negative feedback that partially offsets AMOC-induced cooling. A linear decomposition reveals that this positive CRE arises not from cloud loss, but from a reduction in the cooling efficiency of existing clouds, which more than offsets the enhanced cooling from increased cloud cover. Our findings demonstrate that aerosol–cloud interactions form an active component of the climate response to AMOC weakening, exposing a critical gap in simulations that rely on prescribed aerosol fields.

https://doi.org/10.5194/egusphere-2026-2961
Preprint. Discussion started: 2 June 2026

1 Introduction

The Atlantic Meridional Overturning Circulation (AMOC) plays a central role in the global climate system by redistributing vast quantities of heat from the tropics to the North Atlantic (Siedler et al., 2001). Anthropogenic climate change is driving rapid Arctic warming and ice melt, increasing the influx of freshwater into the North Atlantic (Bamber et al., 2018). This additional freshwater reduces the salinity and density of the upper ocean, weakening deep water formation (Sévellec et al., 2017). As a result, the sinking branch of the AMOC becomes progressively suppressed, and the overturning circulation loses strength (Bakker et al., 2016).

Multiple lines of evidence indicate that the AMOC functions as a tipping element capable of exhibiting hysteresis (Rahmstorf, 1996; Hofmann and Rahmstorf, 2009; Clement and Peterson, 2008; Caesar et al., 2020). A sustained forcing perturbation, such as increased freshwater input, can push the circulation beyond a critical threshold, triggering a transition to a weakened or collapsed state that may persist even after the original forcing is removed. Although the future trajectory of the AMOC remains uncertain (Baker et al., 2025), its potential destabilisation represents one of the most consequential risks to the global climate system (Weijer et al., 2019).

The impacts of a weakening AMOC extend far beyond the Atlantic basin. A reduction in overturning strength attenuates northward heat transport, producing pronounced interhemispheric temperature contrasts and a distinctive warming hole over the subpolar North Atlantic. These thermal anomalies drive a large-scale reorganisation of atmospheric circulation, including a southward shift of the Intertropical Convergence Zone (ITCZ) (Frajka-Williams et al., 2019; Jackson et al., 2022; Ben-Yami et al., 2024). Through global teleconnections, these changes propagate across the climate system, affecting monsoonal rainfall, vegetation distributions, and atmospheric composition (Sandeep et al., 2020; Zickfeld et al., 2008; Vella et al., 2026). Within this cascade of feedbacks, cloud responses remain one of the largest sources of uncertainty (Boucher et al., 2013; Zelinka et al., 2020). Previous studies indicate that AMOC weakening can substantially alter the radiative budget through cloud adjustments. In the tropics, the southward displacement of the ITCZ drives opposing changes in low- and high-level cloud cover, modulating top-of-atmosphere radiative fluxes (Cheng et al., 2007; Drijfhout, 2015). In the mid-latitudes, a weakened AMOC amplifies meridional sea surface temperature (SST) gradients, potentially strengthening the Northern Hemisphere storm track and enhancing low cloud formation (Trossman et al., 2016). Over the North Atlantic warming hole, cooler SSTs enhance lower tropospheric stability and maintain a moister boundary layer, increasing cloud fraction and liquid water path while reducing downward shortwave radiation, thereby amplifying surface cooling (Zhang et al., 2019; Fan et al., 2025; Liu et al., 2023; Drijfhout, 2015).

Most previous studies have focused primarily on thermodynamic and macrophysical cloud responses, leaving a critical gap in our understanding of how aerosol–cloud interactions shape the climate response to AMOC weakening. Changes in atmospheric circulation and surface wind patterns associated with a weakened AMOC inevitably alter natural aerosol emissions as well as their atmospheric transport and processing. Understanding the interplay between these microphysical perturbations and the macrophysical cloud response is therefore essential for accurately constraining the radiative impacts of AMOC weakening. In this study, we examine global cloud adjustments resulting from a 60 % weakening of the AMOC relative to present-day conditions. We employ the ICON-HAM global aerosol–climate model, which explicitly resolves aerosol microphysics, aerosol–cloud interactions, and cloud radiative processes, enabling a self-consistent assessment of how AMOC-driven changes in aerosol distributions propagate into cloud properties and radiative forcing.

2 Model description and methods

2.1 ICON-HAM

ICON-A-HAM2.3 couples the ICOsahedral Non-hydrostatic (ICON) atmospheric general circulation model with the Hamburg Aerosol Module version 2.3 (HAM2.3), providing a global atmosphere–aerosol modelling framework for simulating aerosol processes and their interactions with radiation and clouds (Salzmann et al., 2022). ICON-A denotes the atmosphere component of the ICON Earth system model (Giorgetta et al., 2018; Crueger et al., 2018). The dynamical core solves the non-hydrostatic equations of motion on an icosahedral-triangular Arakawa C grid (Zängl et al., 2015). The physics package originates from the ECHAM6 general circulation model (Stevens et al., 2013) and has been adapted to the ICON framework, with dynamics and physics coupled through a sequential updating approach following a fixed process ordering (Giorgetta et al., 2018).

Aerosol processes are treated using HAM2.3, originally developed within the ECHAM-HAM modelling system (Stier et al., 2005) and subsequently updated by Zhang et al. (2012). HAM simulates the life cycle of five aerosol species: sulfate (SU), black carbon (BC), organic carbon (OC), sea salt (SS), and mineral dust (DU) (Tegen et al., 2019). The aerosol size distribution is represented by the M7 microphysical module (Vignati et al., 2004), which describes the aerosol population as seven interactive lognormal modes, four hydrophilic (nucleation, Aitken, accumulation, and coarse) and three hydrophobic (Aitken, accumulation, and coarse), with prescribed geometric standard deviations but prognostic number median radii. The prognostic variables are the particle number concentration of each mode and the mass concentration of each aerosol compound within that mode. HAM2.3 treats nucleation of sulfate aerosol, condensational growth by gas-phase sulfuric acid, coagulation, as well as emission, transport, and wet and dry deposition (Salzmann et al., 2022). Hydrophobic particles undergo ageing to the hydrophilic population through coagulation with hydrophilic particles or condensation of sulfuric acid (Stier et al., 2005). After each time step, the model redistributes particles among modes to maintain the number median radius within prescribed bounds (Vignati et al., 2004; Stier et al., 2005). Aerosol water uptake is computed within the κ-Köhler framework of Petters and Kreidenweis (2007), as implemented by O'Donnell et al. (2011), and aerosol optical properties are derived from volume-weighted refractive indices and Mie-scattering parameters assuming internal mixing (Stier et al., 2007). Secondary organic aerosol (SOA) formation follows a simplified approach in which approximately 15 % of natural terpene emissions condense immediately onto existing particles at the surface (Dentener et al., 2006; Stier et al., 2005).

The ICON-HAM configuration used here employs a two-moment stratiform cloud microphysics scheme that carries prognostic cloud droplet number concentration (CDNC) and ice crystal number concentration (ICNC) (Lohmann and Roeckner, 1996), with recent improvements documented by Lohmann and Neubauer (2018) and Neubauer et al. (2019). The scheme solves prognostic equations for the mass mixing ratios and number concentrations of cloud droplets and ice crystals, while rain and snow are treated diagnostically (Lohmann and Roeckner, 1996; Lohmann et al., 2007). Cloud droplet activation is parameterised following the Köhler-theory-based approach of Abdul-Razzak and Ghan (2000), which determines the activated fraction as a function of the aerosol size distribution and hygroscopicity provided by HAM, together with the sub-grid updraft velocity. In mixed-phase clouds, mineral dust particles can initiate contact freezing and serve as ice-nucleating particles for immersion freezing (Tegen et al., 2019; Lohmann and Diehl, 2006). Black carbon is also represented as an immersion-freezing INP, although its parameterised efficiency is approximately four orders of magnitude lower than that of dust (montmorillonite). Additional microphysical processes include condensation, evaporation, deposition, sublimation, autoconversion of cloud droplets to rain, accretion, aggregation, riming, and aerosol wet scavenging (Neubauer et al., 2019). Fractional cloud cover is diagnosed from relative humidity following Sundqvist et al. (1989). Convective clouds are parameterised using a mass-flux scheme with moisture convergence closure for shallow and mid-level convection and CAPE-based closure for deep convection (Giorgetta et al., 2018).

2.2 Experimental design

The experimental strategy isolates the atmospheric response to an AMOC-weakened ocean state by prescribing sea surface boundary condition perturbations derived from a fully coupled simulation, while holding all emission sources fixed. Monthly climatological anomalies in sea surface temperature (ΔSST) and sea ice concentration (ΔSIC) were derived from a fully coupled ocean–atmosphere simulation performed with EC-Earth3 (Döscher et al., 2022), following the protocol of the North Atlantic Hosing Model Intercomparison Project (Jackson et al., 2023). In the EC-Earth3 simulation, the AMOC was weakened by imposing a spatially uniform freshwater flux of 0.3 Sv poleward of 50°N over the Atlantic and Arctic Oceans, applied to a pre-industrial background state. From the resulting 140-year transient integration, two quasi-equilibrated states were identified: a control state with a mean AMOC strength of approximately 17.5 Sv and a weakened state of 7.0 Sv, corresponding to a ∼60 % reduction. The monthly climatological ΔSST and ΔSIC fields were computed as the difference between these two states (Fig. 1).

Two ICON-HAM simulations were performed at R2B4 resolution (∼160 km) with 47 vertical levels. Each simulation was initialised on 1 October 1999 and integrated through January 2010; the first three months were discarded as spin-up, yielding 10 years (2000–2009) of analysed output. Both simulations were run in free-running AMIP-style mode without meteorological nudging. The prescribed SST climatology was constructed as a multi-model ensemble mean of year-2015 monthly SSTs from four CMIP6 models run under SSP5-8.5 (CESM2, AWI-CM-1-1MR, HadGEM3-GC31-MM, and GFDL-CM4), remapped to the ICON R2B4 grid and repeated as a perpetual annual cycle. The Control simulation used this unperturbed climatology, while the Hosing simulation superimposed the EC-Earth3-derived ΔSST and ΔSIC anomalies onto the same fields. All anthropogenic and biomass-burning emissions were held fixed at perpetual 2015 levels throughout the integration, ensuring that any changes in aerosol distributions arise solely from dynamical adjustments rather than emission changes. All other boundary conditions were identical between the two experiments.

Ozone concentrations were prescribed from the CMIP6 historical climatology (Hegglin et al., 2016). Greenhouse gas mixing ratios (CO_2, CH_4, N_2O, CFCs) followed the CMIP6 historical dataset (Meinshausen et al., 2017), and solar irradiance was prescribed from the CMIP6 solar forcing dataset (Matthes et al., 2017). Stratospheric volcanic aerosol optical properties followed Stenchikov et al. (1998). Anthropogenic and biomass-burning emissions of BC, OC, SO_2, and DMS were prescribed from the ACCMIP dataset (Lamarque et al., 2010), interpolated to 2015 using the RCP4.5 scenario (Thomson et al., 2011). Continuous and explosive volcanic degassing emissions followed the AEROCOM climatology (Dentener et al., 2006). Dust (Tegen et al., 2002; Cheng et al., 2008) and sea salt (Long et al., 2011) emissions are computed interactively. Land surface processes were represented by JSBACHv4 (Reick et al., 2021) with terrestrial carbon cycling disabled.

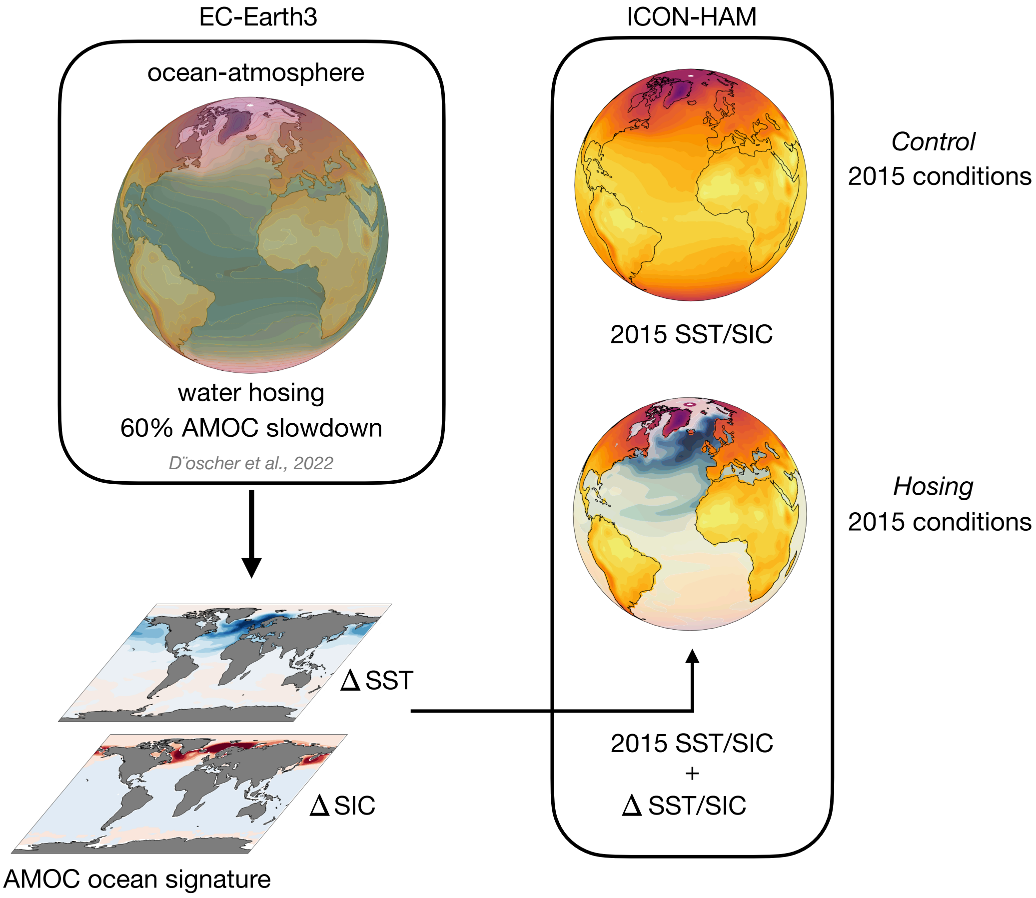

Figure 1. Schematic overview of the experimental design. Anomalies in sea surface temperature (ΔSST) and sea ice concentration (ΔSIC) are derived from a fully coupled EC-Earth3 freshwater-hosing simulation that produces an approximately 60 % reduction in AMOC strength. These anomalies are imposed in ICON-HAM, resulting in two configurations: (i) a present-day Control simulation (2015 climatology) and (ii) a Hosing experiment incorporating the AMOC-induced oceanic perturbation. Image adopted from Vella et al. (2026).

https://doi.org/10.5194/egusphere-2026-2961
Preprint. Discussion started: 2 June 2026

3 Results and Discussion

The climate response to AMOC weakening extends well beyond the direct thermodynamic imprint of North Atlantic cooling. As the large-scale atmospheric circulation reorganises in response to the altered meridional temperature gradient, surface wind patterns, precipitation regimes, and soil moisture distributions adjust accordingly. These dynamical changes influence the emission, transport, and removal of natural aerosol species, thereby reshaping the atmospheric aerosol burden, even in the absence of changes in anthropogenic emissions. In this section, we quantify the climate response, aerosol redistribution, and associated cloud impacts under a 60 % AMOC slowdown relative to present-day conditions.

3.1 Climate response

The freshwater hosing and subsequent 60 % reduction in AMOC strength produce a pronounced hemispheric temperature asymmetry (Fig. 2a). Surface temperatures are reduced by more than 4 K over the subpolar North Atlantic, with statistically significant cooling extending zonally across much of the Northern Hemisphere mid-latitudes. Averaged over the Northern Hemisphere, surface temperature decreases by $\sim$2.3 K, nearly twice the global-mean cooling of $\sim$1.2 K. These values fall within the range reported by the North Atlantic Hosing Model Intercomparison Project (Jackson et al., 2023), where eight CMIP6-class models produced subpolar North Atlantic cooling between 2 and 8 K under comparable freshwater forcing. The NH-mean cooling in our simulations is also broadly in line with the $\sim$0.7 K value reported by Bellomo and Mehling (2024) for a $\sim$10 Sv AMOC weakening under a $4\times CO_2$ background, noting that the larger cooling in our experiment reflects both the greater weakening magnitude and the present-day (rather than warmed) background climate state.

The vertical structure of this thermal perturbation is illustrated by the zonal-mean temperature anomalies (Fig. 2b). Cooling originates near the surface at high northern latitudes, where reduced SSTs and expanded sea ice (Fig. S1) suppress turbulent heat fluxes into the boundary layer (Fan et al., 2025). This cold anomaly propagates upward through the lower and middle troposphere and extends southward, shifting the annual-mean surface 0 °C isotherm from $\sim$58 °N in the Control simulation to $\sim$52 °N under hosing (roughly 710 km southward). A localised warming signal is evident above 60 °N near 200 hPa, likely reflecting changes in eddy heat flux convergence or storm-track dynamics associated with the shifted meridional temperature gradient. Meanwhile, pronounced surface cooling at high northern latitudes, combined with comparatively modest cooling aloft, increases atmospheric stratification in the lower troposphere. This vertical temperature structure, in which boundary-layer cooling enhances static stability, favours the persistence of stratiform cloud layers over the subpolar North Atlantic (Zhang et al., 2010; Fan et al., 2025), with direct consequences for the cloud radiative response discussed in Sect. 3.3.

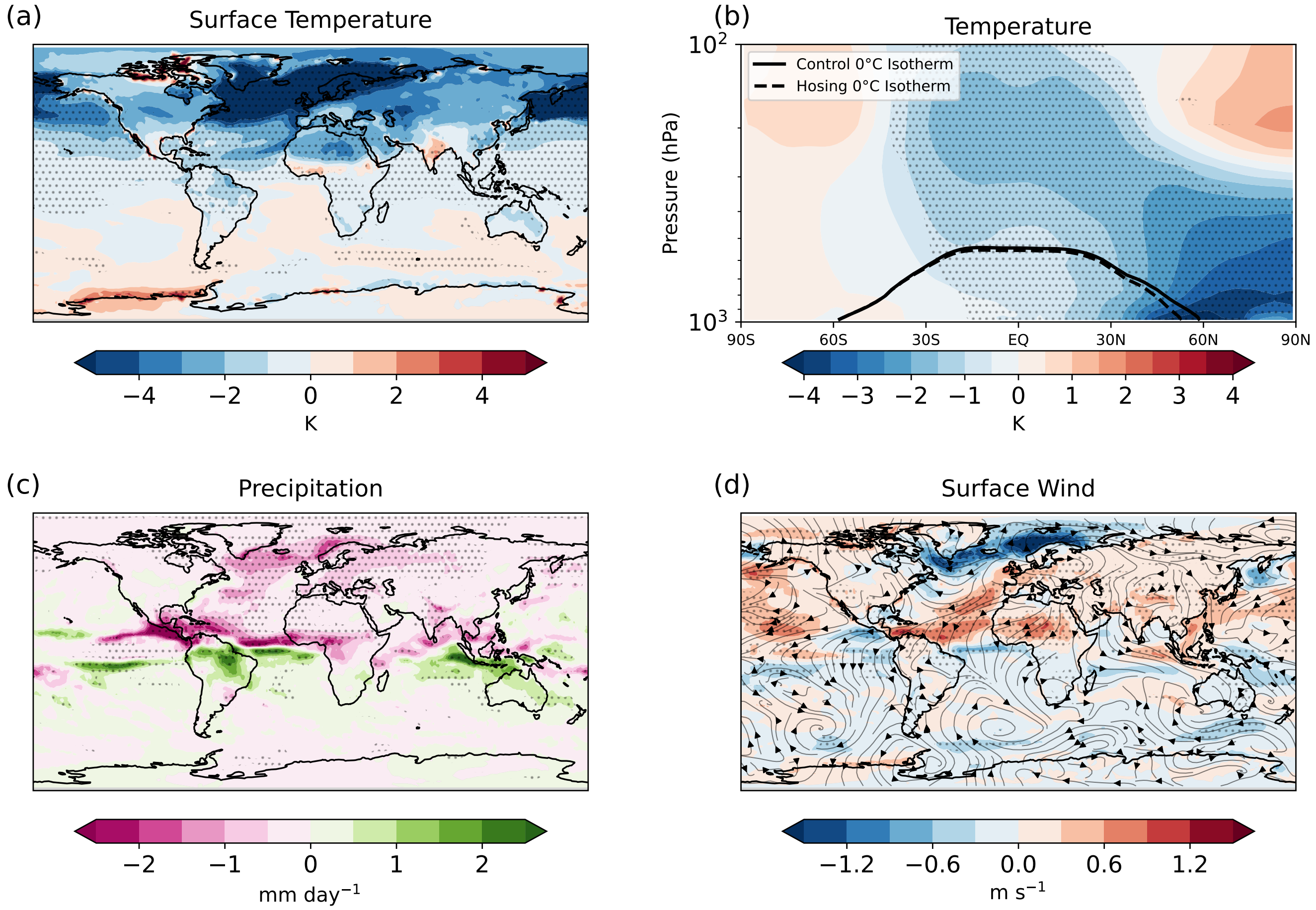

Figure 2. Annual mean climate response to freshwater hosing. (a) surface temperature anomalies, (b) zonal mean vertical temperature anomalies, (c) precipitation anomalies, and (d) surface wind speed and direction anomalies. Anomalies are calculated as the Hosing experiment minus the Control. In panel (b), the solid black line indicates the 0°C isotherm for the Control simulation, while the dashed black line indicates the 0°C isotherm for the Hosing simulation. Stippling indicates regions where the difference is statistically significant at the 95 % confidence level ($p < 0.05$).

The altered meridional thermal gradient drives a fundamental reorganisation of the hydrological cycle (Fig. 2c). Global-mean precipitation decreases by $\sim 0.10\,\mathrm{mm\,day^{-1}}$, but the reduction is strongly concentrated in the Northern Hemisphere ($\sim 0.36\,\mathrm{mm\,day^{-1}}$). The zonal-mean precipitation profiles (Fig. S2) reveal that the NH mid-latitude rain band weakens considerably under hosing, while the SH storm track remains largely unchanged. The strongest drying is concentrated over the North Atlantic, as well as most of western Europe (Fig. 2c). In the tropics, the anomalies exhibit a characteristic dipole with reduced rainfall north of the equator and enhanced rainfall to the south (Fig. S2b), confirming a southward displacement of the ITCZ. This meridional shift represents a dynamical adjustment of the Hadley circulation that transports energy northward across the equator, partially compensating for diminished oceanic heat transport (Frajka-Williams et al., 2019; Jackson et al., 2022; Ben-

Yami et al., 2024). Over South Asia, the monsoon response is characterised by a decline in precipitation, driven by diminished cross-equatorial moisture transport and a southward displacement of the ITCZ (Sandeep et al., 2020; Vella et al., 2026). The extent of this reduction, however, differs markedly among models. For instance, Ben-Yami et al. (2024) demonstrates that Indian Summer Monsoon rainfall decreases by up to an order of magnitude across four state-of-the-art Earth System Models. In this context, the response simulated by ICON-HAM is comparatively weak.

The surface wind response (Fig. 2d) reflects the altered pressure gradients associated with the cooled North Atlantic. Over the subpolar North Atlantic, wind speeds decrease by more than $1.5\,\mathrm{m\,s^{-1}}$ as the surface cooling raises local sea-level pressure and weakens the prevailing westerlies. Conversely, winds strengthen over the subtropical North Atlantic and western Sahara, where the steepened meridional temperature gradient between the cooled mid-latitudes and the comparatively unchanged tropics enhances low-level flow (Orihuela-Pinto et al., 2022).

3.2 Aerosol redistribution

Although anthropogenic emissions remain constant across both simulations, the dynamical adjustments described in Sect. 3.1 drive a substantial spatial redistribution of the global aerosol burden. The yearly mean aerosol burden (Fig. 3a) increases by more than $400\,\mathrm{mg\,m^{-2}}$ over the Sahara and tropical North Atlantic, driven primarily by enhanced dust mobilisation under stronger surface winds (Fig. 2d). The zonal-mean burden (Fig. 3b) peaks at $\sim 190\,\mathrm{mg\,m^{-2}}$ near 15–$20\,^\circ\mathrm{N}$ and tapers off sharply south of the equator.

The species-resolved zonal-mean AOT (Fig. 3d) shows that dust accounts for the largest contribution. Dust emissions from the Sahara increase by $3.7\,\mathrm{mg\,m^{-2}\,day^{-1}}$ ($+8.2\,\%$), and the resulting plume extends westward over the subtropical North Atlantic via the Saharan Air Layer. Globally, the total aerosol column burden increases by $1.22\,\mathrm{mg\,m^{-2}}$ ($+3.8\,\%$). This change is almost entirely confined to the Northern Hemisphere, where the mean burden increases by $2.54\,\mathrm{mg\,m^{-2}}$ ($+5.2\,\%$), while the Southern Hemisphere exhibits a negligible change ($< 1\,\%$). The vertical extent of the aerosol perturbation is illustrated by the zonal-mean particulate matter concentration (Fig. 3e) and extinction coefficient at 550 nm (Fig. 3f). The largest PM increases, exceeding $30\,\mathrm{\mu g\,m^{-3}}$, are concentrated in the tropical lower troposphere between 0–$20\,^\circ\mathrm{N}$ below 800 hPa. The extinction field shows a broader pattern of enhancement, extending from the tropical boundary layer through much of the troposphere at 20–$50\,^\circ\mathrm{N}$.

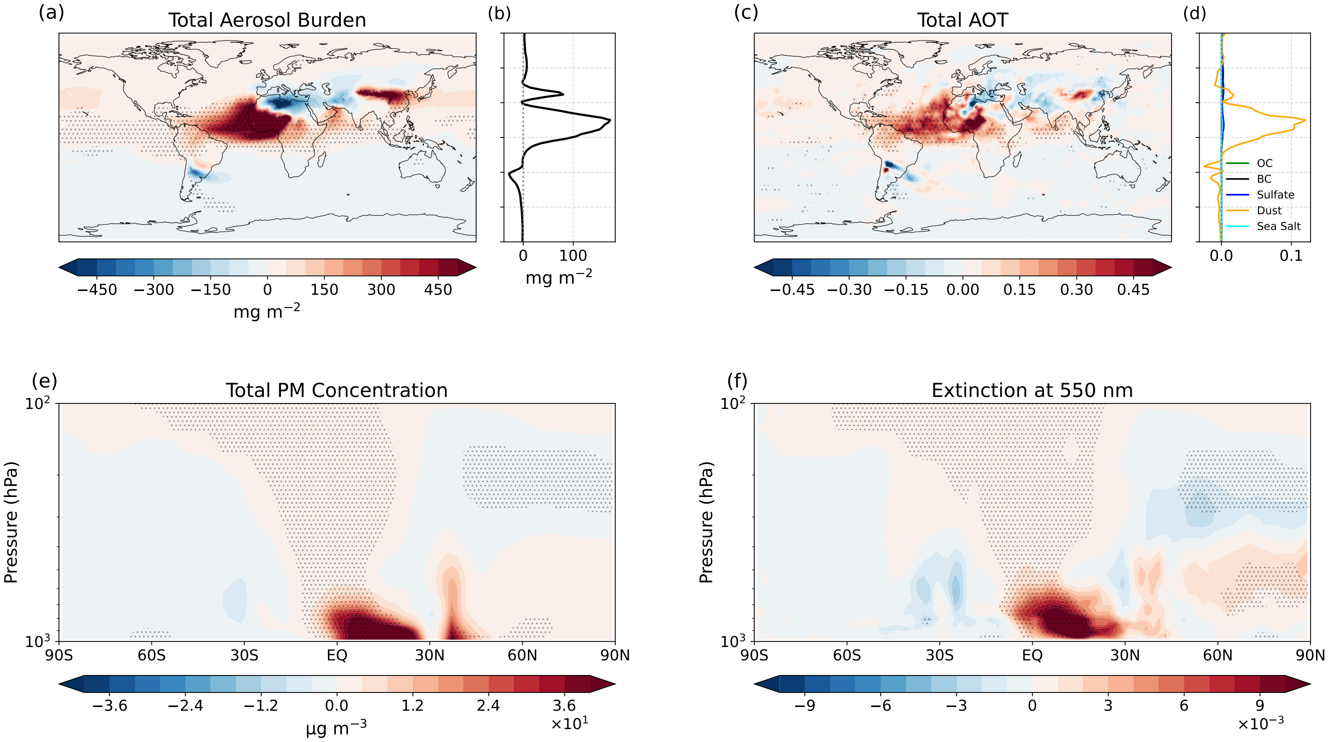

Figure 3. Aerosol response to 60 % AMOC slowdown. (a) Global map of differences in Total Aerosol Burden. (b) Zonal mean of the Total Aerosol Burden differences corresponding to panel (a). (c) Global map of differences in Total Aerosol Optical Thickness (AOT) at 550 nm. (d) Zonal mean differences in AOT at 550 nm separated by individual aerosol components: Organic Carbon (OC), Black Carbon (BC), Sulfate, Dust, and Sea Salt. (e) Zonal mean latitude-pressure cross-section of differences in Total particulate matter (PM) concentration. (f) Zonal mean latitude-pressure cross-section of differences in aerosol Extinction at 550 nm. Stippling indicates regions where the difference is statistically significant at the 95 % confidence level ($p < 0.05$).

The enhanced Saharan dust export finds strong support in the palaeoclimate record. Speleothem and marine sediment reconstructions show that periods of weakened AMOC and increased latitudinal temperature gradients coincide with elevated Saharan dust fluxes (Cruz et al., 2021; Williams et al., 2016). During Heinrich events, when the AMOC weakened to near collapsed states, estimated at roughly 80 to 90 % reductions based on kinematic proxies (McManus et al., 2004), dust deposition rates in Atlantic sediments and the Eastern Mediterranean increased two to fivefold above background levels, driven by stronger surface winds and drier North African conditions (Ehrmann et al., 2017). The 8.2 % increase in Saharan dust emissions simulated here is considerably smaller than these palaeo-reconstructed enhancements, consistent with the partial nature of the imposed weakening (60 % versus near collapse) and the present-day background climate state, which features weaker meridional temperature gradients and more vegetated North African margins than during glacial conditions (Mahowald et al., 1999; Tegen et al., 2002).

The increase in water-soluble aerosol burden despite fixed precursor emissions reveals a second, complementary mechanism. Suppressed Northern Hemisphere rainfall reduces wet scavenging efficiency, extending the atmospheric residence time of sulfate and carbonaceous species. Figure S3 confirms this, showing anomalies in both aerosol mass (Fig. S3a) and number (Fig. S3b) wet deposition. Aerosol mass wet deposition increases sharply over the Sahara and tropical North Atlantic, where the enhanced dust burden provides substantially more material for scavenging. The aerosol number wet deposition field (Fig. S3b) shows a broadly negative pattern across most of the Northern Hemisphere, indicating that fewer aerosol particles are removed per unit time, reflecting the suppressed precipitation documented in Fig. 2c. This precipitation-mediated lifetime feedback is well established in single-forcing experiments (e.g., Croft et al., 2009) and has recently been assessed in the context of AMOC weakening and air quality (Vella et al., 2026).

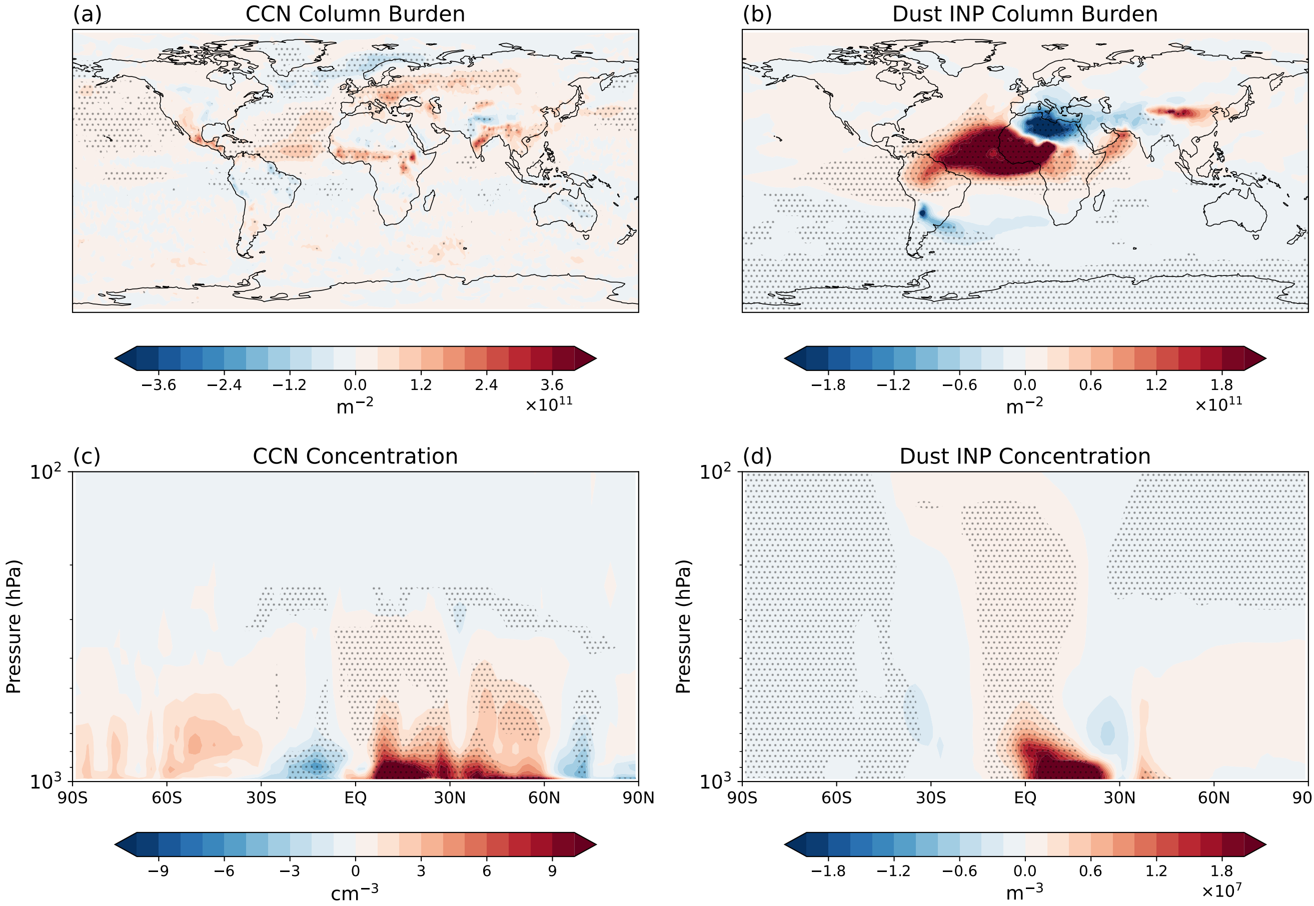

Figure 4. (a) Global map of differences in CCN column burden. (b) Global map of differences in dust INP column burden. (c) Zonal mean latitude-pressure cross-section of differences in CCN Concentration. (d) Zonal mean latitude-pressure cross-section of differences in dust INP concentration. Stippling indicates regions where the difference is statistically significant at the 95 % confidence level ($p < 0.05$).

https://doi.org/10.5194/egusphere-2026-2961
Preprint. Discussion started: 2 June 2026

The aerosol redistribution directly alters the availability of cloud condensation nuclei (CCN) and ice-nucleating particles (INPs). The CCN column burden (Fig. 4a) shows an increase over the mid-Atlantic Ocean, while further north in the Atlantic, CCN column burden decreases. The vertical cross-section (Fig. 4c) confirms that CCN concentrations increase throughout the lower and middle troposphere between the equator and $\sim$40°N, with the largest enhancements below 800 hPa in the NH tropics. At high northern latitudes, CCN concentrations decrease through most of the tropospheric column. The dust INP column burden (Fig. 4b) shows a more spatially confined response, with increases concentrated over North Africa and the tropical North Atlantic. The vertical distribution (Fig. 4d) reveals that dust INP concentrations increase primarily in the lower troposphere between 10–30°N, where the Saharan dust plume is most prominent, and decrease at high latitudes where reduced poleward transport limits dust availability.

3.3 Cloud adjustments

The AMOC-induced changes in temperature, circulation, and aerosol loading produce a complex pattern of cloud adjustments in all cloud levels (Fig. 5). The low cloud response (Fig. 5a) is dominated by a broad increase of $\sim$4–9 % over the North Atlantic, with locally significant anomalies exceeding $+10$ %. The surface cooling discussed in Sect. 3.1 enhances lower-tropospheric stability over the open ocean, suppressing vertical mixing and favouring the formation and persistence of stratiform cloud decks. Large-eddy simulations by Schneider et al. (2019) demonstrate that stratocumulus persistence depends critically on lower-tropospheric stability and cloud-top radiative cooling, and that perturbations to these controls can trigger abrupt transitions in cloud regime. In our simulations, the AMOC-induced surface cooling acts in the stabilising direction, reinforcing stratocumulus formation and stability. This pattern is in agreement with the findings of Fan et al. (2025), who show that enhanced cloud cover over the subpolar North Atlantic reinforces surface cooling under a weakening AMOC, and with Zhang et al. (2019), who link cooler North Atlantic SSTs to increased cloud fraction and liquid water path through enhanced lower-tropospheric stability.

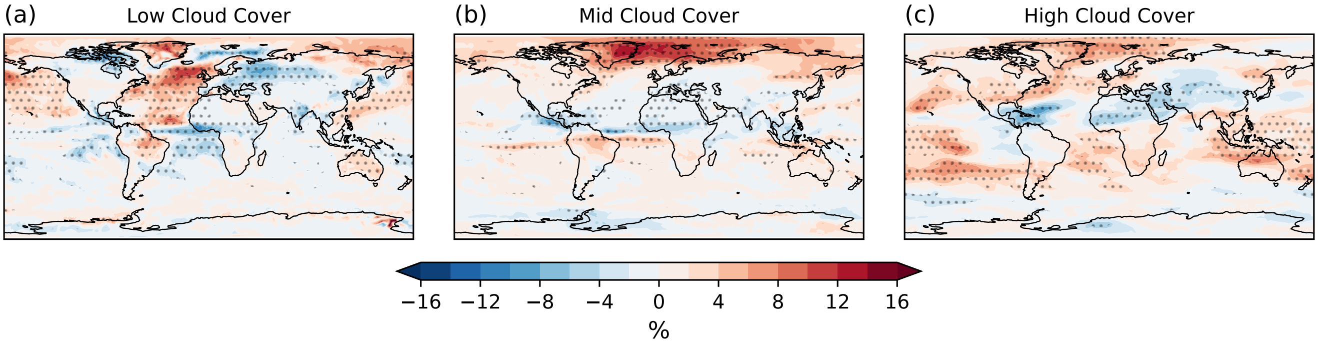

Figure 5. Global maps of differences in (a) Low Cloud Cover (surface to 680 hPa), (b) Mid Cloud Cover (680 hPa to 440 hPa), and (c) High Cloud Cover (above 440 hPa). Stippling indicates regions where the difference is statistically significant at the 95 % confidence level ($p < 0.05$).

Mid-level cloud cover (Fig. 5b) increases by up to $+9$ to $+13\,\%$ over the subpolar North Atlantic and Nordic Seas, with the anomaly extending into northern Europe. In the tropics, the mid-cloud response displays a distinct meridional dipole, with decreases of $\sim$4–9 % north of the equator and increases of similar magnitude to the south, reflecting the southward ITCZ displacement discussed in Sect. 3.1. High cloud cover (Fig. 5c) decreases by $\sim$4–9 % across the tropical North Atlantic, Caribbean, and tropical North Africa, and increases by a comparable amount over the southern tropical Atlantic, and the Maritime Continent. At higher latitudes, high cloud cover increases over parts of northern Europe and the subpolar North Atlantic. The increase in high cloud cover at these latitudes likely reflects enhanced frontal cloud production associated with the strengthened meridional SST gradient and baroclinicity, as well as a lowering of the 0°C isotherm (Fig. 2b) that shifts cloud-top temperatures into colder categories.

The tropical cloud dipole at multiple levels is a robust feature of AMOC weakening experiments. Zhang et al. (2010) demonstrated that AMOC-induced surface cooling increases low cloud cover over the North Atlantic through atmospheric stabilisation, while the southward ITCZ shift produces opposing cloud changes between the hemispheres that amplify the tropical precipitation response. Similar multi-level cloud adjustments following AMOC decline have been reported across a range of coupled models (Liu et al., 2020; Bellomo and Mehling, 2024).

The liquid water path (LWP, Fig. 6a) decreases over the Arctic and continental Eurasia, where surface cooling reduces the moisture available for liquid-phase cloud formation. Over the mid-latitude Atlantic and Pacific oceans, LWP increases by up to $\sim$30–45 $\mathrm{g\,m^{-2}}$, collocated with the enhanced low cloud cover in these regions (Fig. 5a). This LWP increase over the North Atlantic is in agreement with Fan et al. (2025), who find that AMOC weakening enhances liquid water path over the subpolar North Atlantic through a colder, drier boundary layer that strengthens the capping inversion and suppresses precipitation loss from the cloud layer. In the tropics, the LWP anomalies mirror the southward shift of the ITCZ, with reductions north of the equator and increases to the south. The ice water path (Fig. 6b) decreases over the North Atlantic, in agreement with the reduced high cloud cover in this region (Fig. 5c). Increases in IWP are evident over the southern tropical Atlantic, Indian Ocean, and Maritime Continent, tracking the southward-shifted deep convective activity. The opposing LWP and IWP responses over the North Atlantic, with increased liquid water but decreased ice water, are physically coherent with the enhanced lower-tropospheric stability documented in Sect. 3.1, which favours shallow liquid-phase stratiform clouds at the expense of deeper ice-producing convective clouds (Zhang et al., 2010).

https://doi.org/10.5194/egusphere-2026-2961
Preprint. Discussion started: 2 June 2026

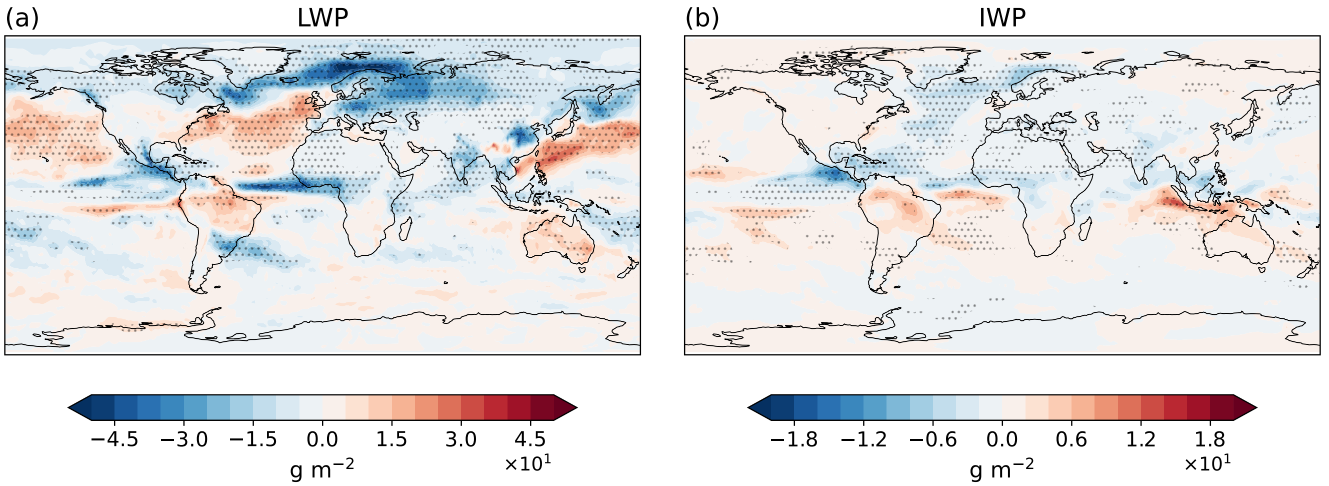

Figure 6. Changes in (a) liquid water path (LWP), (b) ice water path (IWP). Stippling indicates regions where the differences are statistically significant at the 95 % confidence level ($p < 0.05$).

Over the Arctic, the increase in mid- and high-level cloud cover is not accompanied by an IWP increase, because cloud occurrence and cloud condensate are governed by different controls. At mid-levels (440 to 680 hPa), relative humidity rises by 2.7 percentage points even though specific humidity falls ($-0.14\,\mathrm{g\,kg^{-1}}$). This occurs because surface cooling lowers the saturation vapour pressure faster than it removes absolute moisture, pushing the air closer to saturation. The higher RH triggers additional cloud formation through the Sundqvist diagnostic scheme, but the reduced absolute moisture leaves less water available to condense within each cloud. At upper levels (above 440 hPa), cloud fraction increases despite a slight RH decrease (-0.3 percentage points), indicating that the additional cloud is generated dynamically through enhanced frontal lifting under the strengthened meridional temperature gradient, rather than thermodynamically. Underlying both regimes, Arctic-mean surface evaporation weakens by $0.27\,\mathrm{mm\,day^{-1}}$ as expanding sea ice reduces the open-ocean moisture source, limiting condensate supply at all levels. Conditional in-cloud diagnostics (poleward of 60°N) confirm this decoupling. Cloud fraction increases at every level, while in-cloud condensate falls by $1.0\,\mathrm{g\,m^{-2}}$ for mid- and high-level IWP and $27.9\,\mathrm{g\,m^{-2}}$ for low-level LWP. This suggests that more clouds form, but each holds less water.

Most previous studies of AMOC-induced cloud changes have focused on these macrophysical and thermodynamic responses (Trossman et al., 2016; Zhang et al., 2019; Fan et al., 2025; Drijfhout, 2015). A key contribution of this study is to examine whether the aerosol redistribution documented in Sect. 3.2 also influences cloud properties through microphysical pathways. Given the complexity of the simultaneous changes in circulation, thermodynamics, and aerosol distributions, disentangling the aerosol–cloud microphysical response from the macrophysical adjustments on a regional basis is challenging. To isolate the microphysical signal, we bin cloud properties by in-cloud temperature (and cloud-top temperature) using daily instantaneous model output, which removes much of the spatial covariance between thermodynamic regime shifts and aerosol perturbations.

Within a given thermal environment, changes in cloud microphysical properties can then be attributed more directly to aerosol perturbations rather than thermodynamic regime shifts.

Figure 7 illustrates the aerosol–cloud microphysical linkage across the cloud temperature spectrum over 40–90°N, where the AMOC-induced perturbations are strongest. The lines include shading denoting ± 2 standard errors of the mean ($\mathrm{SEM} = \sigma/\sqrt{n}$), however, the envelopes are narrow due to the large sample size n from daily output, gridpoint-level data over the full 10-year period, indicating that the reported mean differences are statistically robust. In the liquid regime (Fig. 7a), CCN concentrations (dashed lines) are elevated in the Hosing simulation relative to the Control, with increases of $5.5\,\%$ in warm clouds ($> 0\,°\mathrm{C}$) and $26.1\,\%$ in the mixed-phase regime (0 to $-35\,°\mathrm{C}$). The in-cloud CDNC response (solid lines) tracks this CCN enhancement but exceeds it in warm clouds, where CDNC increases by $8.4\,\%$ compared with the $5.5\,\%$ CCN increase. The elevated CCN produce additional, individually smaller droplets that collide less efficiently, suppressing autoconversion to rain and allowing CDNC to build up beyond the initial CCN perturbation. This cloud lifetime feedback is consistent with the $+8.1\,\%$ total water path increase in warm clouds (Fig. 7d) and with the strong inverse dependence of the autoconversion rate on CDNC in the Khairoutdinov and Kogan (2000) parameterisation. The $+2.0\,\%$ increase in the activation fraction (Fig. 7c) provides an additional contribution, indicating that a larger fraction of the available aerosol is incorporated into cloud droplets. A spatial diagnostic using daily in-cloud data over the full 10-year period confirms the cloud lifetime feedback across sub-regions. Over 50–65°N, CDNC increases by $+5.2\,\%$ despite only a $+1.8\,\%$ CCN increase, reflecting strong autoconversion suppression with minimal aerosol forcing. Over 30–50°N, where the CCN increase is larger ($+6.2\,\%$), CDNC increases by $+5.0\,\%$, tracking the CCN perturbation more closely as the stronger aerosol source enhances the lifetime signal.

https://doi.org/10.5194/egusphere-2026-2961
Preprint. Discussion started: 2 June 2026

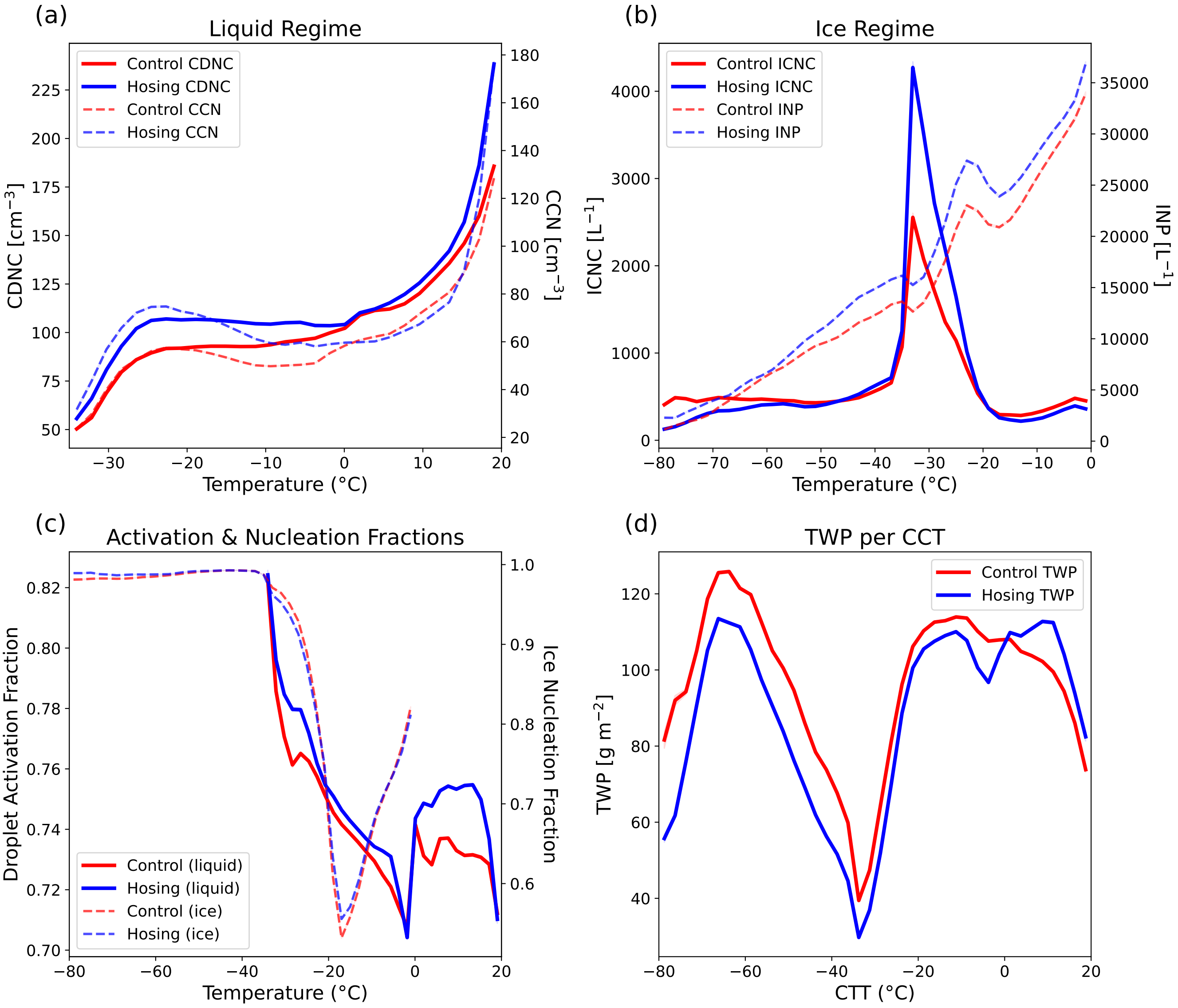

Figure 7. In-cloud microphysical properties as a function of temperature over 40–90°N, derived from daily instantaneous output. (a) Cloud droplet number concentration (CDNC, solid lines, left axis, cm^{-3}) and cloud condensation nuclei concentration (CCN, dashed lines, right axis) as a function of temperature in the liquid cloud regime. (b) Ice crystal number concentration (ICNC, solid lines, left axis) and ice nucleating particle concentration (INP, dashed lines, right axis) as a function of temperature in the ice cloud regime. (c) Droplet activation fraction (solid lines, left axis) and ice nucleation fraction (dashed lines, right axis) as a function of temperature. (d) Total water path (TWP) sorted by cloud-top temperature. In all panels, red lines denote the Control simulation and blue lines denote the Hosing simulation. Shading denotes ±2 standard errors of the mean.

https://doi.org/10.5194/egusphere-2026-2961
Preprint. Discussion started: 2 June 2026

The activation fraction increase is concentrated over the mid-latitude North Atlantic (30–50°N), where reduced wet scavenging extends aerosol residence times, allowing accumulation-mode particles to grow through continued condensation of soluble material and coagulation. The resulting size increase ($+0.8\,\%$ in the median radius of accumulation-mode particles) lowers the critical supersaturation for activation, producing a $+2.8\,\%$ increase in activation fraction. Over 50–65°N, accumulation-mode particles are smaller ($-2.0\,\%$) and the activation fraction is unchanged, indicating that the ageing signal is confined to the mid-latitudes where the precipitation reduction is strongest. The domain-mean vertical velocity over 40–90°N changes by only $9\times10^{-5}\,\mathrm{m\,s^{-1}}$, confirming that dynamical changes play no meaningful role in the activation response.

In the mixed-phase regime, the in-cloud CDNC increase of $13.3\,\%$ is substantially smaller than the $26.1\,\%$ CCN enhancement, even though the activation fraction is roughly unchanged ($+0.9\,\%$). This gap is explained by the Wegener–Bergeron–Findeisen process. The $37.0\,\%$ increase in in-cloud ICNC (Fig. 7b) means substantially more ice crystals compete for water vapour, forcing supercooled droplets to evaporate and reducing the surviving droplet population below what CCN activation alone would produce. In the ice regime (Fig. 7b), dust INP concentrations (dashed lines) increase by $13.1\,\%$ in the mixed-phase temperature range. The in-cloud ICNC response of $+37.0\,\%$ in this regime substantially exceeds the INP perturbation, amplified by the temperature shift in the hosing simulation. The immersion freezing parameterisation of Lohmann and Diehl (2006) uses an empirical fit in which the frozen liquid fraction scales as $\exp(T_{\mathrm{melt}} - T)$, so that a modest cooling produces a large increase in ice formation per INP. Contact freezing efficiency increases linearly with supercooling through a temperature-dependent collection kernel. The combination of more INPs and colder nucleation temperatures produces the approximately 2.8-fold amplification of the ICNC response relative to the INP perturbation. In the cirrus regime, in-cloud ICNC decreases by $14.0\,\%$ despite an $18.6\,\%$ increase in dust INP. Since heterogeneous nucleation is not enabled for cirrus in this ICON-HAM configuration, this reduction reflects a shift in the altitude of cirrus formation rather than aerosol perturbations. Enhanced lower-tropospheric stability suppresses the deepest convective towers, shifting cirrus occurrence to lower, warmer altitudes. The cloud-top temperature distribution (Fig. S4) confirms a reorganisation within the ice cloud regime, showing that the sharp Control peak near $-70\,°\mathrm{C}$ is flattened under hosing, with cloud occurrence redistributed toward both colder tops (-80 to $-85\,°\mathrm{C}$) and moderately cold tops near $-55\,°\mathrm{C}$. The net effect is a broadening of the cirrus CTT distribution, shifting the population-weighted mean formation temperature toward warmer values where homogeneous freezing nucleation rates are lower, producing fewer ice crystals per cloud event.

The activation and nucleation fractions (Fig. 7c) provide insight into the efficiency of aerosol incorporation into cloud condensate. The droplet activation fraction increases by $2.0\,\%$ in warm clouds and $0.9\,\%$ in the mixed-phase regime. The fact that the activation fraction increases in both regimes despite elevated CCN concentrations indicates that the additional aerosol particles are being activated at comparable or marginally higher efficiency, rather than competing for the available supersaturation. The ice nucleation fraction (dashed lines, right axis) is unchanged in the mixed-phase regime and is negligible in the cirrus regime ($+0.3\,\%$), consistent with the dominance of homogeneous freezing below $-35\,°\mathrm{C}$ in the model's ice nucleation scheme. The unchanged mixed-phase nucleation fraction, combined with the amplified ICNC response ($+37.0\,\%$), confirms that the amplification is driven by colder nucleation temperatures rather than a higher fraction of INPs freezing. Figure 7d shows the mean TWP as a function of cloud-top temperature, the average condensate loading per cloud within each thermal regime. Clouds with the coldest tops (CTT < -60 °C) carry the most water because they span a deep atmospheric column, whereas warm shallow clouds (CTT > 0 °C) carry far less. The high values at -70 °C reflect deep convective systems with ice-dominated upper portions rather than optically thin cirrus, which would carry much less water.

Within this structure, the Hosing simulation produces regime-dependent shifts. Warm clouds (> 0 °C) show a TWP increase of $8.1\,\%$, consistent with the elevated CDNC documented in Fig. 7a. More numerous droplets are individually smaller, reducing the collision-coalescence efficiency that drives autoconversion to rain (Albrecht, 1989). In the mixed-phase regime (0 to -35 °C), TWP decreases by $7.9\,\%$, indicating that the enhanced WBF process leads to precipitation and thinning of the clouds. The $37.0\,\%$ increase in in-cloud ICNC, driven by enhanced dust-derived INP availability (Sect. 3.2) and colder nucleation temperatures, promotes ice crystal growth at the expense of supercooled liquid droplets via the WBF process (Korolev, 2007).

Cold clouds (< -35 °C) exhibit the largest TWP decrease ($17.0\,\%$), visible in Fig. 7d as the Hosing curve falling below the Control between approximately -40 and -60 °C. In this regime, ice formation is governed by homogeneous freezing, and the total condensate is controlled primarily by moisture supply and updraft strength. Enhanced lower-tropospheric stability under hosing suppresses the deepest convective towers, shifting cirrus formation to lower, warmer altitudes where homogeneous freezing nucleation rates are lower. This CTT-shift mechanism explains both the $14.0\,\%$ ICNC decrease and the $17.0\,\%$ TWP decrease. Fewer ice crystals nucleate at the warmer formation temperatures, and the shallower cloud columns contain less vertically integrated condensate.

3.4 Radiative effects

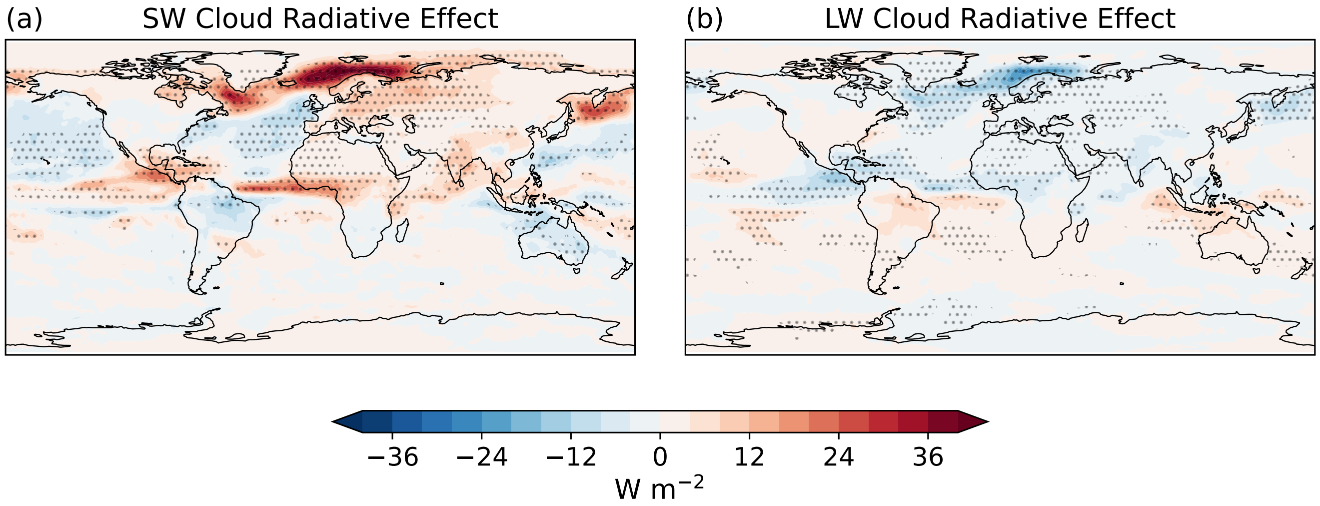

Figure 8. Global maps of differences in (a) Shortwave (SW) Cloud Radiative Effect, (b) Longwave (LW) Cloud Radiative Effect. Stippling indicates regions where the difference is statistically significant at the 95 % confidence level ($p < 0.05$).

https://doi.org/10.5194/egusphere-2026-2961
Preprint. Discussion started: 2 June 2026

The shortwave and longwave cloud radiative effects (Fig. 8) summarise the net radiative consequences of the cloud changes documented above. The SW cloud radiative effect (Fig. 8a) becomes more negative by 24 to 36 $\mathrm{W\,m^{-2}}$ over the North Atlantic, where increased low and mid-level cloud cover (Fig. 5a,b) and higher cloud optical thickness from elevated CDNC enhance cloud albedo. Over the tropical North Atlantic and Caribbean, the SW effect is positive ($+12$ to $+24\,\mathrm{W\,m^{-2}}$), reflecting the reduction in cloud cover associated with the southward shift of the ITCZ. A positive ΔSW CRE is also evident over the Arctic, where sea ice expansion (Fig. S1) eliminates the open-ocean moisture source and suppresses low cloud formation (Fig. 5a), reducing shortwave reflection by clouds. This Arctic cloud response to AMOC-driven sea ice changes is in agreement with Lee et al. (2024), who find that a weakened AMOC reduces low-level cloud fraction over the Arctic sea ice margins via shortwave cloud feedback. The LW cloud radiative effect (Fig. 8b) shows a broad negative anomaly (-12 to $-24\,\mathrm{W\,m^{-2}}$) over the tropical North Atlantic, Africa, and South Asia, where the southward ITCZ shift and reduced high cloud cover (Fig. 5c) decrease the longwave trapping by clouds. Globally, the area-weighted SW cloud radiative effect anomaly is $+1.16\,\mathrm{W\,m^{-2}}$, indicating a net reduction in cloud reflectivity, while the LW cloud radiative effect anomaly is $-0.32\,\mathrm{W\,m^{-2}}$. The SW component therefore dominates, yielding a net cloud radiative effect anomaly of $+0.84\,\mathrm{W\,m^{-2}}$ that acts as a negative feedback on the AMOC-induced surface cooling.

To identify the mechanism behind the positive global-mean ΔNet CRE, we decompose the anomaly at each grid cell into cloud fraction and in-cloud contributions:

$$\Delta\mathrm{CRE} \approx \underbrace{\Delta f \times \overline{\mathrm{CRE}}_{\mathrm{ctrl}}}_{\text{cloud fraction term}} + \underbrace{f_{\mathrm{ctrl}} \times \Delta\overline{\mathrm{CRE}}}_{\text{in-cloud term}} \tag{1}$$

where f is total cloud fraction and $\overline{\mathrm{CRE}} = \mathrm{CRE}/f$ is the in-cloud CRE. The cloud fraction term ($-0.66\,\mathrm{W\,m^{-2}}$) indicates that the widespread increase in cloud cover documented in Sect. 3.3 would, in isolation, enhance planetary cooling. However, this is more than offset by the in-cloud term ($+1.43\,\mathrm{W\,m^{-2}}$), which shows that existing clouds become optically thinner. This in-cloud weakening arises from the TWP decreases in the mixed-phase ($-7.9\,\%$) and ice cloud ($-17.0\,\%$) regimes. The warm cloud TWP increase ($+8.1\,\%$) partially counteracts this reduction, but the mixed-phase and cold cloud regimes carry substantially more condensate per cloud and span a larger fraction of the global cloud population, so their TWP decreases dominate the in-cloud term. The two linear terms sum to $+0.77\,\mathrm{W\,m^{-2}}$, with the remaining $+0.07\,\mathrm{W\,m^{-2}}$ of the directly diagnosed $+0.84\,\mathrm{W\,m^{-2}}$ anomaly arising from the nonlinear cross term ($\Delta f \times \Delta\overline{\mathrm{CRE}}$) neglected in Eq. (1). The net positive anomaly is therefore driven not by cloud loss, but by a reduction in the cooling efficiency of the cloud population as a whole. This agrees with the TOA radiation anomalies reported by Drijfhout (2015) following AMOC collapse and with the finding of Bellomo and Mehling (2024) that the global-mean radiative response to AMOC weakening is small but masks regional contrasts.

To further disentangle how different cloud regimes contribute to the radiative response, we decompose the cloud radiative effect as a function of CTT using daily instantaneous output (Fig. 9), with SW CRE restricted to daytime grid cells to avoid dilution by nighttime values. In the absolute SW CRE (Fig. 9a), both simulations reach $-220\,\mathrm{W\,m^{-2}}$ at the coldest cloud tops ($\mathrm{CTT} < -80\,^{\circ}\mathrm{C}$), with a secondary minimum of $-170\,\mathrm{W\,m^{-2}}$ near -5 to $0\,^{\circ}\mathrm{C}$ corresponding to optically thick mixed-phase and liquid-topped stratiform clouds. SW CRE weakens to around $-70\,\mathrm{W\,m^{-2}}$ for the warmest cloud tops ($\mathrm{CTT} > 15\,^{\circ}\mathrm{C}$), reflecting the lower optical thickness of shallow boundary-layer clouds. The LW CRE (Fig. 9b) shows the strongest longwave warming effect (∼80–90 $\mathrm{W\,m^{-2}}$) from the coldest cloud tops, decreasing monotonically to ∼2–4 $\mathrm{W\,m^{-2}}$ for the shallowest warm clouds. The net CRE (Fig. 9c) is negative across all CTT bins in both simulations, with an absolute minimum of around $-150\,\mathrm{W\,m^{-2}}$ near CTTs of $0\,°\mathrm{C}$, where optically thick stratiform clouds produce strong SW cooling with only modest LW compensation, and a secondary minimum of around $-135\,\mathrm{W\,m^{-2}}$ at the coldest cloud tops (CTT $< -80\,°\mathrm{C}$). Fig. S4 shows the CTT distribution for both simulations, normalised by the total number of cloudy grid cells. The distribution is bimodal, with one peak near CTTs of $-60\,°\mathrm{C}$ in the ice/cirrus regime and a second peak near CTTs of 0 to $+5\,°\mathrm{C}$ corresponding to warm boundary-layer clouds. The mixed-phase regime (-35 to $0\,°\mathrm{C}$) represents a relative minimum in cloud occurrence. The Hosing experiment slightly reduces the occurrence of the coldest cloud tops (CTT $< -65\,°\mathrm{C}$) while increasing the fraction near $-55\,°\mathrm{C}$, suggesting a shift within the ice cloud regime toward moderately cold clouds at the expense of the deepest convective towers. The warm cloud peak remains largely unchanged between the two simulations.

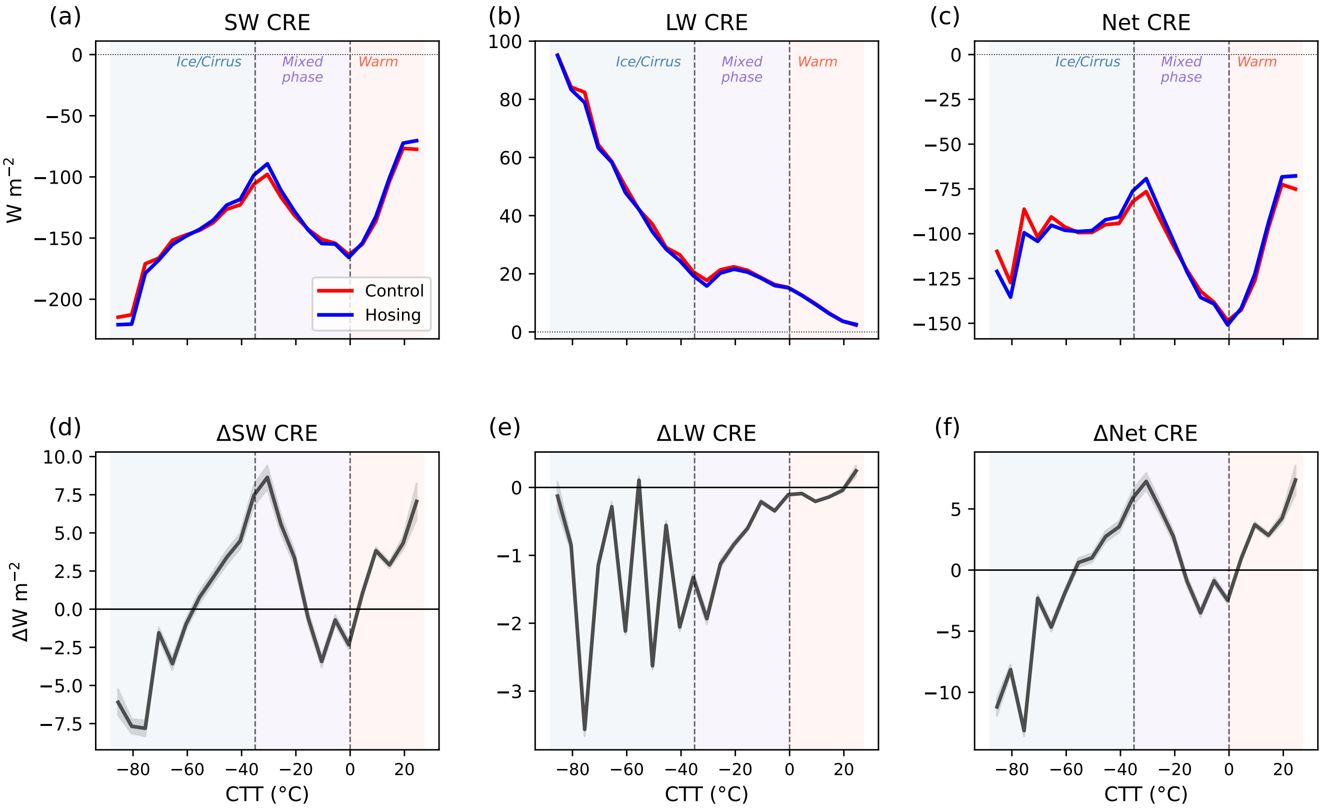

Figure 9. Absolute values of (a) Shortwave (SW) CRE, (b) Longwave (LW) CRE, and (c) Net CRE as a function of cloud-top temperature for the Control (blue lines) and Hosing (red lines) simulations. Differences (Hosing minus Control) in (d) SW CRE, (e) LW CRE, and (f) Net CRE. All quantities are derived from daily instantaneous output, with SW CRE restricted to daytime grid cells to avoid dilution by nighttime values. Shading denotes ±2 standard errors of the mean.

https://doi.org/10.5194/egusphere-2026-2961
Preprint. Discussion started: 2 June 2026

The ΔSW CRE (Fig. 9d) reveals a complex, regime-dependent pattern. The coldest cloud tops (CTT $< -75\,°\mathrm{C}$) show strongly negative anomalies reaching approximately $-7.8\,\mathrm{W\,m^{-2}}$, driven by increased cloud optical thickness over the subpolar North Atlantic. The anomaly then increases steadily with CTT, crossing zero near $-57\,°\mathrm{C}$ and becoming strongly positive across the warmer ice/cirrus and colder mixed-phase regimes, where it peaks at about $+8.5\,\mathrm{W\,m^{-2}}$ near the $-35\,°\mathrm{C}$ boundary, reflecting reduced cloud optical thickness. The positive anomaly declines with further warming and crosses zero near $-15\,°\mathrm{C}$, and ΔSW CRE remains negative through the warmer mixed-phase regime, with a local minimum of about $-3.5\,\mathrm{W\,m^{-2}}$ near $-11\,°\mathrm{C}$. For the warmest cloud tops (CTT $> 0\,°\mathrm{C}$), ΔSW CRE is again positive, rising to roughly $+7\,\mathrm{W\,m^{-2}}$ at the warmest tops, indicating reduced shortwave cooling from the shallowest boundary-layer clouds. This is consistent with the decrease in low cloud cover over the tropical North Atlantic and Arctic (Fig. 5a), where the southward ITCZ shift and sea ice expansion reduce shallow cloud occurrence. The ΔLW CRE (Fig. 9e) is negative across nearly all CTT bins, with the largest contributions from the ice/cirrus regime (-2 to $-3.5\,\mathrm{W\,m^{-2}}$), where reduced cloud occurrence and lower cloud-top heights decrease longwave trapping. Near the warmest cloud tops, ΔLW CRE approaches zero, as expected for shallow clouds emitting at temperatures close to the surface.

The net CRE perturbation (Fig. 9f) exhibits pronounced sign changes across the temperature spectrum. The coldest cloud tops (CTT $< -70\,°\mathrm{C}$) produce strongly negative anomalies of -10 to $-12\,\mathrm{W\,m^{-2}}$, where the SW and LW perturbations reinforce each other. Near $-35\,°\mathrm{C}$ the anomaly turns positive ($\sim +5\,\mathrm{W\,m^{-2}}$), as the positive ΔSW CRE outweighs the negative ΔLW contribution, before returning to negative values near $0\,°\mathrm{C}$ ($\sim -3\,\mathrm{W\,m^{-2}}$), where optically thick stratiform clouds become more reflective under hosing. At the warmest cloud tops (CTT $> 10\,°\mathrm{C}$), Δnet CRE is positive again (up to $+8\,\mathrm{W\,m^{-2}}$), driven by reduced shallow cloud occurrence over the tropical North Atlantic and Arctic where the ITCZ shift and sea ice expansion suppress boundary-layer cloud formation. This alternating sign structure shows that the radiative adjustment to AMOC weakening is not concentrated in any single regime but is distributed unevenly across the cloud spectrum, arising from the combined effect of regional cloud-cover changes, microphysical adjustments, and shifts in the cloud-top temperature distribution.

4 Conclusions

In this work, we show that a 60 % AMOC weakening drives a hemispheric redistribution of natural aerosols through purely dynamical pathways, even in the absence of changes in anthropogenic emissions. Enhanced Saharan dust emissions and extended aerosol lifetimes under suppressed wet deposition increase the Northern Hemisphere aerosol burden by 5 %. These aerosol perturbations propagate into cloud properties through both liquid and ice-phase microphysical pathways. Averaged over 40–90°N, in-cloud CDNC increases exceed the CCN perturbation in warm clouds, as suppressed autoconversion allows droplet number to build up beyond what activation alone would produce. In the mid-latitudes (30–50°N), an increase in the droplet activation fraction, driven by a shift toward larger accumulation-mode particles under extended aerosol lifetimes, provides an additional contribution. In the mixed-phase regime, a strongly amplified ICNC response to enhanced dust INP, driven by the exponential temperature dependence of immersion freezing, promotes the WBF process, depleting supercooled liquid water and reducing total water path. In the cirrus regime, ICNC decreases despite increased dust INP, as enhanced lower-tropospheric stability broadens the cirrus formation temperature distribution, shifting the population-weighted mean toward warmer altitudes where homogeneous freezing nucleation rates are lower.

The global-mean net cloud radiative effect anomaly of $+0.84\,\mathrm{W\,m^{-2}}$ acts as a negative feedback that partially offsets AMOC-induced surface cooling. A linear decomposition reveals that this positive anomaly arises not from cloud loss, but from a reduction in the cooling efficiency of existing clouds, driven by decreased condensate in the mixed-phase and cold cloud regimes that more than offsets the enhanced cooling from increased cloud cover. The cloud-top temperature decomposition further reveals that the global-mean anomaly is a small residual of large, opposing contributions from different cloud regimes, implying that the sign of the net cloud feedback is sensitive to the relative representation of deep convective, mixed-phase, and boundary-layer clouds.

These responses are broadly consistent with previous coupled-model studies of AMOC weakening, both in the magnitude of Northern Hemisphere cooling (Jackson et al., 2023; Bellomo and Mehling, 2024) and in the macrophysical cloud adjustments over the subpolar North Atlantic and the tropics (Zhang et al., 2010; Fan et al., 2025; Drijfhout, 2015), while the enhanced Saharan dust export is qualitatively supported by palaeoclimate reconstructions from weak-AMOC intervals (Cruz et al., 2021; McManus et al., 2004). The key advance of this study is to show that aerosol-driven microphysical pathways are an active part of the cloud response in their own right, operating alongside the established thermodynamic and macrophysical adjustments.

We also note some limitations of our experimental design. The atmosphere-only configuration with prescribed sea surface temperature and sea ice, derived from a separate coupled model, excludes ocean–atmosphere feedbacks, so that the cloud and aerosol radiative anomalies diagnosed here cannot, in turn, modify sea surface temperatures or the evolution of the AMOC itself. Holding all emissions fixed against a present-day background, with no concurrent greenhouse warming, means our results isolate the purely mechanistic link between AMOC weakening and aerosol–cloud interactions rather than a realistic future trajectory in which emissions and background climate co-evolve. Nevertheless, in this work, we provide evidence that aerosol–cloud interactions form an active component of the climate response to AMOC weakening, a pathway that models relying on prescribed aerosol fields cannot represent, and whose absence may contribute to the spread in projected climate responses to future AMOC change.

Code and data availability. The ICOsahedral Nonhydrostatic model (ICON) is publicly available to the scientific community via the ICON model website (https://icon-model.org). The simulations in this study were performed using ICON version 2.6.4 (pre open-source version), corresponding to commit `8b144b8bfdc01c8ba1d423de4ecf46e20e1b6527`. The Aerosol–cloud microphysics model HAM is publicly available as part of the HAMMOZ modelling framework (https://git.iac.ethz.ch/hammoz/hammoz).

The model outputs relevant to this study and scripts used to produce all figures are permanently stored in the Zenodo repository and are accessible via .

Author contributions. RV conceptualised the study, prepared the model setup, conducted the simulations, and analysed the model output. UL contributed to the interpretation of the results and supervised the project. RV wrote the manuscript, with input from UL.

Competing interests. The authors have no competing interests to declare.

Acknowledgements. The model simulations were performed on the Santis vCluster of the Alps research infrastructure at the Swiss National Supercomputing Centre (CSCS), with support from ETH Zurich. The journal processing fees were covered by ETH Zurich.

References

Abdul-Razzak, H. and Ghan, S. J.: A Parameterization of Aerosol Activation: 2. Multiple Aerosol Types, Journal of Geophysical Research: Atmospheres, 105, 6837–6844, https://doi.org/10.1029/1999JD901161, 2000.

Albrecht, B. A.: Aerosols, Cloud Microphysics, and Fractional Cloudiness, Science, 245, 1227–1230, https://doi.org/10.1126/science.245.4923.1227, 1989.

Baker, J. A., Bell, M. J., Jackson, L. C., Vallis, G. K., Watson, A. J., and Wood, R. A.: Continued Atlantic Overturning Circulation Even under Climate Extremes, Nature, 638, 987–994, https://doi.org/10.1038/s41586-024-08544-0, 2025.

Bakker, P., Schmittner, A., Lenaerts, J. T. M., Abe-Ouchi, A., Bi, D., van den Broeke, M. R., Chan, W.-L., Hu, A., Beadling, R. L., Marsland, S. J., Mernild, S. H., Saenko, O. A., Swingedouw, D., Sullivan, A., and Yin, J.: Fate of the Atlantic Meridional Overturning Circulation: Strong Decline under Continued Warming and Greenland Melting, Geophysical Research Letters, 43, 12,252–12,260, https://doi.org/10.1002/2016GL070457, 2016.

Bamber, J. L., Tedstone, A. J., King, M. D., Howat, I. M., Enderlin, E. M., van den Broeke, M. R., and Noel, B.: Land Ice Freshwater Budget of the Arctic and North Atlantic Oceans: 1. Data, Methods, and Results, Journal of Geophysical Research: Oceans, 123, 1827–1837, https://doi.org/10.1002/2017JC013605, 2018.

Bellomo, K. and Mehling, O.: Impacts and State-Dependence of AMOC Weakening in a Warming Climate, Geophysical Research Letters, 51, e2023GL107 624, https://doi.org/10.1029/2023GL107624, 2024.

Ben-Yami, M., Good, P., Jackson, L. C., Crucifix, M., Hu, A., Saenko, O., Swingedouw, D., and Boers, N.: Impacts of AMOC Collapse on Monsoon Rainfall: A Multi-Model Comparison, Earth's Future, 12, e2023EF003 959, https://doi.org/10.1029/2023EF003959, 2024.

Boucher, O., Randall, D., Artaxo, P., Bretherton, C., Feingold, G., Forster, P., Kerminen, V.-M., Kondo, Y., Liao, H., Lohmann, U., Rasch, P., Satheesh, S. K., Sherwood, S., Stevens, B., and Zhang, X. Y.: Clouds and Aerosols, in: Climate Change 2013: The Physical Science Basis, pp. 571–657, Cambridge University Press, https://doi.org/10.1017/CBO9781107415324.016, 2013.

Caesar, L., Rahmstorf, S., and Feulner, G.: On the Relationship between Atlantic Meridional Overturning Circulation Slowdown and Global Surface Warming, Environmental Research Letters, 15, 024 003, https://doi.org/10.1088/1748-9326/ab63e3, 2020.

Cheng, T., Peng, Y., Feichter, J., and Tegen, I.: An Improvement on the Dust Emission Scheme in the Global Aerosol-Climate Model ECHAM5-HAM, Atmospheric Chemistry and Physics, 8, 1105–1117, https://doi.org/10.5194/acp-8-1105-2008, 2008.

Cheng, W., Bitz, C. M., and Chiang, J. C. H.: Adjustment of the Global Climate to an Abrupt Slowdown of the Atlantic Meridional Overturning Circulation, in: Ocean Circulation: Mechanisms and Impacts—Past and Future Changes of Meridional Overturning, pp. 295–313, American Geophysical Union (AGU), https://doi.org/10.1029/173GM19, 2007.

Clement, A. C. and Peterson, L. C.: Mechanisms of Abrupt Climate Change of the Last Glacial Period, Reviews of Geophysics, 46, https://doi.org/10.1029/2006RG000204, 2008.

Croft, B., Lohmann, U., Martin, R. V., Stier, P., Wurzler, S., Feichter, J., Posselt, R., and Ferrachat, S.: Aerosol Size-Dependent below-Cloud Scavenging by Rain and Snow in the ECHAM5-HAM, Atmospheric Chemistry and Physics, 9, 4653–4675, https://doi.org/10.5194/acp-9-4653-2009, 2009.

Crueger, T., Giorgetta, M. A., Brokopf, R., Esch, M., Fiedler, S., Hohenegger, C., Kornblueh, L., Mauritsen, T., Nam, C., Naumann, A. K., Peters, K., Rast, S., Roeckner, E., Sakradzija, M., Schmidt, H., Vial, J., Vogel, R., and Stevens, B.: ICON-A, The Atmosphere Component of the ICON Earth System Model: II. Model Evaluation, Journal of Advances in Modeling Earth Systems, 10, 1638–1662, https://doi.org/10.1029/2017MS001233, 2018.

Cruz, J. A., McDermott, F., Turrero, M. J., Edwards, R. L., and Martín-Chivelet, J.: Strong Links between Saharan Dust Fluxes, Monsoon Strength, and North Atlantic Climate during the Last 5000 Years, Science Advances, 7, eabe6102, https://doi.org/10.1126/sciadv.abe6102, 2021.

Dentener, F., Kinne, S., Bond, T., Boucher, O., Cofala, J., Generoso, S., Ginoux, P., Gong, S., Hoelzemann, J. J., Ito, A., Marelli, L., Penner, J. E., Putaud, J.-P., Textor, C., Schulz, M., van der Werf, G. R., and Wilson, J.: Emissions of Primary Aerosol and Precursor Gases in the Years 2000 and 1750 Prescribed Data-Sets for AeroCom, Atmospheric Chemistry and Physics, 6, 4321–4344, https://doi.org/10.5194/acp-6-4321-2006, 2006.

Döscher, R., Acosta, M., Alessandri, A., Anthoni, P., Arsouze, T., Bergman, T., Bernardello, R., Boussetta, S., Caron, L.-P., Carver, G., Castrillo, M., Catalano, F., Cvijanovic, I., Davini, P., Dekker, E., Doblas-Reyes, F. J., Docquier, D., Echevarria, P., Fladrich, U., Fuentes-Franco, R., Gröger, M., v. Hardenberg, J., Hieronymus, J., Karami, M. P., Keskinen, J.-P., Koenigk, T., Makkonen, R., Massonnet, F., Ménégoz, M., Miller, P. A., Moreno-Chamarro, E., Nieradzik, L., van Noije, T., Nolan, P., O'Donnell, D., Ollinaho, P., van den Oord, G., Ortega, P., Prims, O. T., Ramos, A., Reerink, T., Rousset, C., Ruprich-Robert, Y., Le Sager, P., Schmith, T., Schrödner, R., Serva, F., Sicardi, V., Sloth Madsen, M., Smith, B., Tian, T., Tourigny, E., Uotila, P., Vancoppenolle, M., Wang, S., Wårlind, D., Willén, U., Wyser, K., Yang, S., Yepes-Arbós, X., and Zhang, Q.: The EC-Earth3 Earth System Model for the Coupled Model Intercomparison Project 6, Geoscientific Model Development, 15, 2973–3020, https://doi.org/10.5194/gmd-15-2973-2022, 2022.

Drijfhout, S. S.: Global Radiative Adjustment after a Collapse of the Atlantic Meridional Overturning Circulation, Climate Dynamics, 45, 1789–1799, https://doi.org/10.1007/s00382-014-2433-9, 2015.

Ehrmann, W., Schmiedl, G., Beuscher, S., and Krüger, S.: Intensity of African Humid Periods Estimated from Saharan Dust Fluxes, PLOS ONE, 12, e0170 989, https://doi.org/10.1371/journal.pone.0170989, 2017.

Fan, Y., Chan, D., Clothiaux, E. E., Zhang, P., and Li, L.: Subpolar North Atlantic Cooling Reinforced by Colder, Drier Atmosphere with a Weakening Atlantic Meridional Overturning Circulation, Science Advances, 11, eads1624, https://doi.org/10.1126/sciadv.ads1624, 2025.

Frajka-Williams, E., Ansorge, I. J., Baehr, J., Bryden, H. L., Chidichimo, M. P., Cunningham, S. A., Danabasoglu, G., Dong, S., Donohue, K. A., Elipot, S., Heimbach, P., Holliday, N. P., Hummels, R., Jackson, L. C., Karstensen, J., Lankhorst, M., Le Bras, I. A., Lozier, M. S., McDonagh, E. L., Meinen, C. S., Mercier, H., Moat, B. I., Perez, R. C., Piecuch, C. G., Rhein, M., Srokosz, M. A., Trenberth, K. E., Bacon, S., Forget, G., Goni, G., Kieke, D., Koelling, J., Lamont, T., McCarthy, G. D., Mertens, C., Send, U., Smeed, D. A., Speich, S., van den Berg, M., Volkov, D., and Wilson, C.: Atlantic Meridional Overturning Circulation: Observed Transport and Variability, Frontiers in Marine Science, 6, https://doi.org/10.3389/fmars.2019.00260, 2019.

Giorgetta, M. A., Brokopf, R., Crueger, T., Esch, M., Fiedler, S., Helmert, J., Hohenegger, C., Kornblueh, L., Köhler, M., Manzini, E., Mauritsen, T., Nam, C., Raddatz, T., Rast, S., Reinert, D., Sakradzija, M., Schmidt, H., Schneck, R., Schnur, R., Silvers, L., Wan, H., Zängl, G., and Stevens, B.: ICON-A, the Atmosphere Component of the ICON Earth System Model: I. Model Description, Journal of Advances in Modeling Earth Systems, 10, 1613–1637, https://doi.org/10.1029/2017MS001242, 2018.

Hegglin, M., Kinnison, D., Lamarque, J.-F., and Plummer, D.: CCMI ozone in support of CMIP6 - version 1.0, https://doi.org/10.22033/ESGF/input4MIPs.1115, 2016.

Hofmann, M. and Rahmstorf, S.: On the Stability of the Atlantic Meridional Overturning Circulation, Proceedings of the National Academy of Sciences, 106, 20 584–20 589, https://doi.org/10.1073/pnas.0909146106, 2009.

Jackson, L. C., Biastoch, A., Buckley, M. W., Desbruyères, D. G., Frajka-Williams, E., Moat, B., and Robson, J.: The Evolution of the North Atlantic Meridional Overturning Circulation since 1980, Nature Reviews Earth & Environment, 3, 241–254, https://doi.org/10.1038/s43017-022-00263-2, 2022.

Jackson, L. C., Alastrué de Asenjo, E., Bellomo, K., Danabasoglu, G., Haak, H., Hu, A., Jungclaus, J., Lee, W., Meccia, V. L., Saenko, O., Shao, A., and Swingedouw, D.: Understanding AMOC Stability: The North Atlantic Hosing Model Intercomparison Project, Geoscientific Model Development, 16, 1975–1995, https://doi.org/10.5194/gmd-16-1975-2023, 2023.

Khairoutdinov, M. and Kogan, Y.: A New Cloud Physics Parameterization in a Large-Eddy Simulation Model of Marine Stratocumulus, Monthly Weather Review, 128, 229–243, https://doi.org/10.1175/1520-0493(2000)128<0229:ANCPPI>2.0.CO;2, 2000.

Korolev, A.: Limitations of the Wegener–Bergeron–Findeisen Mechanism in the Evolution of Mixed-Phase Clouds, Journal of the Atmospheric Sciences, 64, 3372–3375, https://doi.org/10.1175/JAS4035.1, 2007.

Lamarque, J.-F., Bond, T. C., Eyring, V., Granier, C., Heil, A., Klimont, Z., Lee, D., Liousse, C., Mieville, A., Owen, B., Schultz, M. G., Shindell, D., Smith, S. J., Stehfest, E., Van Aardenne, J., Cooper, O. R., Kainuma, M., Mahowald, N., McConnell, J. R., Naik, V., Riahi, K., and van Vuuren, D. P.: Historical (1850–2000) Gridded Anthropogenic and Biomass Burning Emissions of Reactive Gases and Aerosols: Methodology and Application, Atmospheric Chemistry and Physics, 10, 7017–7039, https://doi.org/10.5194/acp-10-7017-2010, 2010.

Lee, Y.-C., Liu, W., Fedorov, A. V., Feldl, N., and Taylor, P. C.: Impacts of Atlantic Meridional Overturning Circulation Weakening on Arctic Amplification, Proceedings of the National Academy of Sciences, 121, e2402322 121, https://doi.org/10.1073/pnas.2402322121, 2024.

Liu, W., Fedorov, A. V., Xie, S.-P., and Hu, S.: Climate Impacts of a Weakened Atlantic Meridional Overturning Circulation in a Warming Climate, Science Advances, 6, eaaz4876, https://doi.org/10.1126/sciadv.aaz4876, 2020.

Liu, W., Duarte Cavalcante Pinto, D., Fedorov, A., and Zhu, J.: The Impacts of a Weakened Atlantic Meridional Overturning Circulation on ENSO in a Warmer Climate, Geophysical Research Letters, 50, e2023GL103 025, https://doi.org/10.1029/2023GL103025, 2023.

Lohmann, U. and Diehl, K.: Sensitivity Studies of the Importance of Dust Ice Nuclei for the Indirect Aerosol Effect on Stratiform Mixed-Phase Clouds, Journal of the Atmospheric Sciences, 63, 968–982, https://doi.org/10.1175/JAS3662.1, 2006.

Lohmann, U. and Neubauer, D.: The Importance of Mixed-Phase and Ice Clouds for Climate Sensitivity in the Global Aerosol–Climate Model ECHAM6-HAM2, Atmospheric Chemistry and Physics, 18, 8807–8828, https://doi.org/10.5194/acp-18-8807-2018, 2018.

Lohmann, U. and Roeckner, E.: Design and Performance of a New Cloud Microphysics Scheme Developed for the ECHAM General Circulation Model, Climate Dynamics, 12, 557–572, https://doi.org/10.1007/BF00207939, 1996.

Lohmann, U., Stier, P., Hoose, C., Ferrachat, S., Kloster, S., Roeckner, E., and Zhang, J.: Cloud Microphysics and Aerosol Indirect Effects in the Global Climate Model ECHAM5-HAM, Atmospheric Chemistry and Physics, 7, 3425–3446, https://doi.org/10.5194/acp-7-3425-2007, 2007.

Long, M. S., Keene, W. C., Kieber, D. J., Erickson, D. J., and Maring, H.: A Sea-State Based Source Function for Size- and Composition-Resolved Marine Aerosol Production, Atmospheric Chemistry and Physics, 11, 1203–1216, https://doi.org/10.5194/acp-11-1203-2011, 2011.

Mahowald, N., Kohfeld, K., Hansson, M., Balkanski, Y., Harrison, S. P., Prentice, I. C., Schulz, M., and Rodhe, H.: Dust Sources and Deposition during the Last Glacial Maximum and Current Climate: A Comparison of Model Results with Paleodata from Ice Cores and Marine Sediments, Journal of Geophysical Research: Atmospheres, 104, 15 895–15 916, https://doi.org/10.1029/1999JD900084, 1999.

Matthes, K., Funke, B., Andersson, M. E., Barnard, L., Beer, J., Charbonneau, P., Clilverd, M. A., Dudok de Wit, T., Haberreiter, M., Hendry, A., Jackman, C. H., Kretzschmar, M., Kruschke, T., Kunze, M., Langematz, U., Marsh, D. R., Maycock, A. C., Misios, S., Rodger, C. J., Scaife, A. A., Seppälä, A., Shangguan, M., Sinnhuber, M., Tourpali, K., Usoskin, I., van de Kamp, M., Verronen, P. T., and Versick, S.: Solar Forcing for CMIP6 (v3.2), Geoscientific Model Development, 10, 2247–2302, https://doi.org/10.5194/gmd-10-2247-2017, 2017.

McManus, J. F., Francois, R., Gherardi, J.-M., Keigwin, L. D., and Brown-Leger, S.: Collapse and Rapid Resumption of Atlantic Meridional Circulation Linked to Deglacial Climate Changes, Nature, 428, 834–837, https://doi.org/10.1038/nature02494, 2004.

Meinshausen, M., Vogel, E., Nauels, A., Lorbacher, K., Meinshausen, N., Etheridge, D. M., Fraser, P. J., Montzka, S. A., Rayner, P. J., Trudinger, C. M., Krummel, P. B., Beyerle, U., Canadell, J. G., Daniel, J. S., Enting, I. G., Law, R. M., Lunder, C. R., O'Doherty, S., Prinn, R. G., Reimann, S., Rubino, M., Velders, G. J. M., Vollmer, M. K., Wang, R. H. J., and Weiss, R.: Historical Greenhouse Gas Concentrations for Climate Modelling (CMIP6), Geoscientific Model Development, 10, 2057–2116, https://doi.org/10.5194/gmd-10-2057-2017, 2017.

Neubauer, D., Ferrachat, S., Siegenthaler-Le Drian, C., Stier, P., Partridge, D. G., Tegen, I., Bey, I., Stanelle, T., Kokkola, H., and Lohmann, U.: The Global Aerosol–Climate Model ECHAM6.3–HAM2.3 – Part 2: Cloud Evaluation, Aerosol Radiative Forcing, and Climate Sensitivity, Geoscientific Model Development, 12, 3609–3639, https://doi.org/10.5194/gmd-12-3609-2019, 2019.

O'Donnell, D., Tsigaridis, K., and Feichter, J.: Estimating the Direct and Indirect Effects of Secondary Organic Aerosols Using ECHAM5-HAM, Atmospheric Chemistry and Physics, 11, 8635–8659, https://doi.org/10.5194/acp-11-8635-2011, 2011.

Orihuela-Pinto, B., England, M. H., and Taschetto, A. S.: Interbasin and Interhemispheric Impacts of a Collapsed Atlantic Overturning Circulation, Nature Climate Change, 12, 558–565, https://doi.org/10.1038/s41558-022-01380-y, 2022.

Petters, M. D. and Kreidenweis, S. M.: A Single Parameter Representation of Hygroscopic Growth and Cloud Condensation Nucleus Activity, Atmospheric Chemistry and Physics, 7, 1961–1971, https://doi.org/10.5194/acp-7-1961-2007, 2007.

Rahmstorf, S.: On the Freshwater Forcing and Transport of the Atlantic Thermohaline Circulation, Climate Dynamics, 12, 799–811, https://doi.org/10.1007/s003820050144, 1996.

Reick, C. H., Gayler, V., Goll, D., Hagemann, S., Heidkamp, M., Nabel, J. E. M. S., Raddatz, T., Roeckner, E., Schnur, R., and Wilkenskjeld, S.: JSBACH 3 - The Land Component of the MPI Earth System Model: Documentation of Version 3.2, https://doi.org/10.17617/2.3279802, 2021.

Salzmann, M., Ferrachat, S., Tully, C., Münch, S., Watson-Parris, D., Neubauer, D., Siegenthaler-Le Drian, C., Rast, S., Heinold, B., Crueger, T., Brokopf, R., Mülmenstädt, J., Quaas, J., Wan, H., Zhang, K., Lohmann, U., Stier, P., and Tegen, I.: The Global Atmosphere-aerosol Model ICON-A-HAM2.3–Initial Model Evaluation and Effects of Radiation Balance Tuning on Aerosol Optical Thickness, Journal of Advances in Modeling Earth Systems, 14, e2021MS002 699, https://doi.org/10.1029/2021MS002699, 2022.

Sandeep, N., Swapna, P., Krishnan, R., Farneti, R., Prajeesh, A. G., Ayantika, D. C., and Manmeet, S.: South Asian Monsoon Response to Weakening of Atlantic Meridional Overturning Circulation in a Warming Climate, Climate Dynamics, 54, 3507–3524, https://doi.org/10.1007/s00382-020-05180-y, 2020.

Schneider, T., Kaul, C. M., and Pressel, K. G.: Possible Climate Transitions from Breakup of Stratocumulus Decks under Greenhouse Warming, Nature Geoscience, 12, 163–167, https://doi.org/10.1038/s41561-019-0310-1, 2019.

Sévellec, F., Fedorov, A. V., and Liu, W.: Arctic Sea-Ice Decline Weakens the Atlantic Meridional Overturning Circulation, Nature Climate Change, 7, 604–610, https://doi.org/10.1038/nclimate3353, 2017.

Siedler, G., Church, J., and Gould, J., eds.: Ocean Circulation and Climate: Observing and Modelling the Global Ocean, vol. 77 of *International Geophysics Series*, Academic Press, 2001.

Stenchikov, G. L., Kirchner, I., Robock, A., Graf, H.-F., Antuña, J. C., Grainger, R. G., Lambert, A., and Thomason, L.: Radiative Forcing from the 1991 Mount Pinatubo Volcanic Eruption, Journal of Geophysical Research: Atmospheres, 103, 13 837–13 857, https://doi.org/10.1029/98JD00693, 1998.

Stevens, B., Giorgetta, M., Esch, M., Mauritsen, T., Crueger, T., Rast, S., Salzmann, M., Schmidt, H., Bader, J., Block, K., Brokopf, R., Fast, I., Kinne, S., Kornblueh, L., Lohmann, U., Pincus, R., Reichler, T., and Roeckner, E.: Atmospheric Component of the MPI-M Earth System Model: ECHAM6, Journal of Advances in Modeling Earth Systems, 5, 146–172, https://doi.org/10.1002/jame.20015, 2013.

Stier, P., Feichter, J., Kinne, S., Kloster, S., Vignati, E., Wilson, J., Ganzeveld, L., Tegen, I., Werner, M., Balkanski, Y., Schulz, M., Boucher, O., Minikin, A., and Petzold, A.: The Aerosol-Climate Model ECHAM5-HAM, Atmospheric Chemistry and Physics, 5, 1125–1156, https://doi.org/10.5194/acp-5-1125-2005, 2005.

Stier, P., Seinfeld, J. H., Kinne, S., and Boucher, O.: Aerosol Absorption and Radiative Forcing, Atmospheric Chemistry and Physics, 7, 5237–5261, https://doi.org/10.5194/acp-7-5237-2007, 2007.

Sundqvist, H., Berge, E., and Kristjánsson, J. E.: Condensation and Cloud Parameterization Studies with a Mesoscale Numerical Weather Prediction Model, Monthly Weather Review, 117, 1641–1657, https://doi.org/10.1175/1520-0493(1989)117<1641:CACPSW>2.0.CO;2, 1989.

Tegen, I., Harrison, S. P., Kohfeld, K., Prentice, I. C., Coe, M., and Heimann, M.: Impact of Vegetation and Preferential Source Areas on Global Dust Aerosol: Results from a Model Study, Journal of Geophysical Research: Atmospheres, 107, AAC 14–1–AAC 14–27, https://doi.org/10.1029/2001JD000963, 2002.

Tegen, I., Neubauer, D., Ferrachat, S., Siegenthaler-Le Drian, C., Bey, I., Schutgens, N., Stier, P., Watson-Parris, D., Stanelle, T., Schmidt, H., Rast, S., Kokkola, H., Schultz, M., Schroeder, S., Daskalakis, N., Barthel, S., Heinold, B., and Lohmann, U.: The Global Aerosol–Climate Model ECHAM6.3–HAM2.3 – Part 1: Aerosol Evaluation, Geoscientific Model Development, 12, 1643–1677, https://doi.org/10.5194/gmd-12-1643-2019, 2019.

Thomson, A. M., Calvin, K. V., Smith, S. J., Kyle, G. P., Volke, A., Patel, P., Delgado-Arias, S., Bond-Lamberty, B., Wise, M. A., Clarke, L. E., and Edmonds, J. A.: RCP4.5: A Pathway for Stabilization of Radiative Forcing by 2100, Climatic Change, 109, 77, https://doi.org/10.1007/s10584-011-0151-4, 2011.

Trossman, D. S., Palter, J. B., Merlis, T. M., Huang, Y., and Xia, Y.: Large-Scale Ocean Circulation-Cloud Interactions Reduce the Pace of Transient Climate Change, Geophysical Research Letters, 43, 3935–3943, https://doi.org/10.1002/2016GL067931, 2016.

Vella, R., Steil, B., Meccia, V., Tost, H., Lelieveld, J., and Pozzer, A.: Air Quality Penalty in Southeast Asia Driven by AMOC Slowdown, Geophysical Research Letters, 53, e2025GL121 309, https://doi.org/10.1029/2025GL121309, 2026.

Vignati, E., Wilson, J., and Stier, P.: M7: An Efficient Size-Resolved Aerosol Microphysics Module for Large-Scale Aerosol Transport Models, Journal of Geophysical Research: Atmospheres, 109, https://doi.org/10.1029/2003JD004485, 2004.

Weijer, W., Cheng, W., Drijfhout, S. S., Fedorov, A. V., Hu, A., Jackson, L. C., Liu, W., McDonagh, E. L., Mecking, J. V., and Zhang, J.: Stability of the Atlantic Meridional Overturning Circulation: A Review and Synthesis, Journal of Geophysical Research: Oceans, 124, 5336–5375, https://doi.org/10.1029/2019JC015083, 2019.

Williams, R. H., McGee, D., Kinsley, C. W., Ridley, D. A., Hu, S., Fedorov, A., Tal, I., Murray, R. W., and deMenocal, P. B.: Glacial to Holocene Changes in Trans-Atlantic Saharan Dust Transport and Dust-Climate Feedbacks, Science Advances, 2, e1600 445, https://doi.org/10.1126/sciadv.1600445, 2016.

Zängl, G., Reinert, D., Rípodas, P., and Baldauf, M.: The ICON (ICOsahedral Non-hydrostatic) Modelling Framework of DWD and MPI-M: Description of the Non-Hydrostatic Dynamical Core, Quarterly Journal of the Royal Meteorological Society, 141, 563–579, https://doi.org/10.1002/qj.2378, 2015.

Zelinka, M. D., Myers, T. A., McCoy, D. T., Po-Chedley, S., Caldwell, P. M., Ceppi, P., Klein, S. A., and Taylor, K. E.: Causes of Higher Climate Sensitivity in CMIP6 Models, Geophysical Research Letters, 47, e2019GL085 782, https://doi.org/10.1029/2019GL085782, 2020.

Zhang, K., O'Donnell, D., Kazil, J., Stier, P., Kinne, S., Lohmann, U., Ferrachat, S., Croft, B., Quaas, J., Wan, H., Rast, S., and Feichter, J.: The Global Aerosol-Climate Model ECHAM-HAM, Version 2: Sensitivity to Improvements in Process Representations, Atmospheric Chemistry and Physics, 12, 8911–8949, https://doi.org/10.5194/acp-12-8911-2012, 2012.

Zhang, R., Kang, S. M., and Held, I. M.: Sensitivity of Climate Change Induced by the Weakening of the Atlantic Meridional Overturning Circulation to Cloud Feedback, Journal of Climate, 23, 378–389, https://doi.org/10.1175/2009JCLI3118.1, 2010.

Zhang, R., Sutton, R., Danabasoglu, G., Kwon, Y.-O., Marsh, R., Yeager, S. G., Amrhein, D. E., and Little, C. M.: A Review of the Role of the Atlantic Meridional Overturning Circulation in Atlantic Multidecadal Variability and Associated Climate Impacts, Reviews of Geophysics, 57, 316–375, https://doi.org/10.1029/2019RG000644, 2019.

Zickfeld, K., Eby, M., and Weaver, A. J.: Carbon-Cycle Feedbacks of Changes in the Atlantic Meridional Overturning Circulation under Future Atmospheric CO2, Global Biogeochemical Cycles, 22, https://doi.org/10.1029/2007GB003118, 2008.